




Low-cost solutions for mobile passive radar based on multichannel DPCA and NULA configurations

Andrea Quirini , Giovanni Paolo Blasone, Fabiola Colone and Pierfrancesco Lombardo

DIET Department, Sapienza University of Rome, Rome, Italy

Research Paper

Cite this article: Quirini A, Blasone GP, Colone F, Lombardo P (2024). Low-cost solutions for mobile passive radar based on multichannel DPCA and NULA configurations. *International Journal of Microwave and Wireless Technologies* 1–16. <https://doi.org/10.1017/S1759078724000035>

Received: 23 June 2023
Revised: 14 December 2023
Accepted: 31 December 2023

Keywords:

clutter cancellation; moving platform; multichannel DPCA; nonuniform linear arrays; passive radar; radar

Corresponding author: Andrea Quirini;
Email: andrea.quirini@uniroma1.it

Abstract

In this paper, we investigate low-cost solutions for enabling ground moving target indication applications with multichannel mobile passive radar systems. As known, in order to be competitive with their active counterparts, passive radars are typically characterized by severe constraints in terms of cost, complexity, and compactness, especially when installed on moving platforms. On the one hand, carrying out the computations onboard requires processing techniques as simple as possible. On the other hand, the need for lightweight and compact systems that can be installed on a moving platform requires using a limited number of receiving channels. To meet these requirements, we propose a series of nonadaptive detectors based on multichannel displaced phase center antennas, which allow suppressing the Doppler-spread clutter component without requiring computationally intensive space–time adaptive processing techniques. Moreover, we explore the use of nonuniformly spaced array configurations on receive, which represent a good alternative to conventional uniform linear arrays when a limited number of receiving channels can be implemented. The effectiveness of the proposed processing techniques and antenna design solutions is demonstrated via numerical analysis for the case of a DVB-T-based mobile passive radar system.

Introduction

In the last years, there has been significant interest in passive radar systems installed on moving platforms, as evidenced by several studies appeared in the open literature (e.g., see [1–13]). As is well known, passive radar is a receive-only system that allows to detect targets by parasitically exploiting existing transmitters as illuminators of opportunity. This principle of operation brings in a number of advantages including reduced complexity, low probability of intercept, and ease of deployment, [14, 15]. The use of passive radar onboard airborne or ground moving platforms provides enhanced strategic advantages by extending the functionalities of passive radar to applications such as synthetic aperture radar (SAR) imaging [2–4] or ground moving target indication (GMTI) [5–13].

Such systems pose stimulating challenges in terms of both system design and processing techniques. One of the major concerns is that the detection of slow-moving targets is severely degraded by the platform motion, which induces an angle-dependent Doppler component in the clutter signal. To tackle this issue, space–time clutter suppression techniques involving platform motion compensation must be exploited. Typically, the spatial information is provided by the N elements of a multichannel receiving antenna, while the M pulses in the coherent processing interval (CPI) serve as temporal information.

The easiest space–time clutter suppression technique is displaced phase center antennas (DPCAs), which requires an antenna with just two receiving elements [16]. The idea is to compensate the platform motion by subtracting the signals received by the two antenna elements at the time instants in which their phase centers occupy the same positions. The echoes from moving targets are preserved due to their own radial motion, while the contribution from stationary scatterers cancels out. Clearly, this approach requires the pulse repetition frequency (PRF) to be synchronized with the platform velocity, so that the second antenna occupies the position of the first one after an integer number of pulses.

A more advanced approach involving adaptive space–time clutter suppression was formerly introduced by Brennan and Reed in [17] back in 1973 and is usually referred to as space–time adaptive processing (STAP). In the following years, the research on STAP has drawn the attention of several experts in the field (e.g., see [18–20]). STAP is essentially a generalization of DPCA in which the pulses received by an arbitrary number of receiving elements are

© The Author(s), 2024. Published by Cambridge University Press in association with the European Microwave Association. This is an Open Access article, distributed under the terms of the Creative Commons Attribution licence (<http://creativecommons.org/licenses/by/4.0>), which permits unrestricted re-use, distribution and reproduction, provided the original article is properly cited.

combined adaptively, based on the statistical properties of clutter scene. Thanks to its adaptivity, STAP is generally considered more robust than DPCA to nonideal conditions, such as rapid changes in the clutter scene or platform velocity perturbations. Moreover, the higher number of receiving elements provides additional degrees of freedom, which is beneficial to the detection of slow-moving targets. This is especially true when the antennas are positioned strategically, resorting to nonuniform sensor distributions.

However, we note that the improved performance of STAP is achieved at the expenses of a drastically higher computational load. As a matter of fact, STAP is based on the estimation and inversion of the clutter covariance matrix (CCM), which makes practical implementation challenging, especially when a high number of antennas and pulses is used. To tackle this issue, several reduced-order suboptimal STAP techniques have been proposed, which are usually referred to as partially adaptive STAP. An extensive review of fully adaptive STAP and its suboptimal variants can be found in [18].

Although STAP techniques are well-established and their effectiveness has been extensively demonstrated in the open literature, their high complexity does not make them best suited to mobile passive radar applications. Specifically, when dealing with passive radars installed on moving platforms, the designer should always recall that:

- (1) the simplest processing schemes should generally be favored in order to guarantee that the required computations can be carried out onboard;
- (2) key features such as weightlessness and compactness should be pursued, being crucial for the design of easily deployable systems, which can eventually be installed on a moving platform.

To properly address these requirements, in this paper, we work on two different but entwined fronts. On the one hand, the need for simple processing schemes suggests avoiding adaptive filtering techniques altogether, favoring nonadaptive ones. In this perspective, a multichannel DPCA-like solution might represent a convenient, undemanding alternative to reduced-order STAP approaches. On the other hand, the need to preserve ease of deployment fosters the use of lightweight and compact systems that in turn allow a limited number of receiving channels to be featured. To this end, we explore the use of radar receivers based on nonuniform linear array (NULA) configurations, as a way to reduce the number of receiving channels without compromising performance.

Preliminary results along the lines described above have been reported in our previous studies [11–13]. Specifically, in [11], we introduced a nonadaptive solution, referred to as “apodization approach,” in which we exploited three nonuniformly spaced receiving antennas installed on a moving platform to detect moving targets against clutter and noise.

In this paper, we significantly extend the results in [11] by deriving a series of low-complexity nonadaptive detectors based on different signal models, effectively implementing DPCA schemes possibly operating with any number of channels on receive. Furthermore, we characterize the performance of each detector in terms of false alarm probability and detection probability, via both theoretical and simulated analyses. Finally, the advantages and the limitations of nonuniform sensors spacings are investigated when exploiting the proposed detectors with different array layouts.

The remainder of this paper is organized as follows: in “System geometry and signal model”, we present the assumed system

geometry and the signal model adopted. The multichannel DPCA detectors are introduced in “Nonadaptive multichannel DPCA”, and their target detection performance against clutter and noise are evaluated and compared. In “NULA configurations”, these detectors are tested considering both ULA (uniform linear array) and NULA configurations, to point out the advantages of nonuniform sensor spacings. In “Case study: passive radar system based on DVB-T”, the proposed NULA-based multichannel DPCA solutions are tested in a simulated environment, considering the case study of a passive radar system parasitically exploiting digital video broadcasting – terrestrial (DVB-T) transmissions as signals of opportunity. Finally, in “Conclusions”, we draw our conclusions.

System geometry and signal model

In this section, we introduce the assumed system geometry and signal model, constituting the foundation for the derivation of the multichannel DPCA detectors.

System geometry and reference scenario

The system geometry is sketched in Fig. 1. We consider a passive radar system parasitically exploiting continuous wave (CW) transmissions as signals of opportunity. The exploited transmitter (Tx) is assumed to be ground-based and stationary, while the radar receiver (Rx) is installed on a platform located at height H_p and moving at a constant velocity v_p along the direction of the y -axis. The Rx is based on an N -element linear array, also aligned along the y -axis (namely in side-looking configuration). The antenna indices are ordered such that $n = 0$ denotes the leading antenna and $n = N - 1$ denotes the trailing antenna. Let \mathbf{z} be the vector describing the array layout:

$$\mathbf{z} = [d_0, d_1, \dots, d_{N-1}] \lambda, \quad (1)$$

where d_n being the distance of the n th antenna from the leading antenna in λ units ($0 = d_0 < d_1 < \dots < d_{N-1}$).

When CW transmissions are employed as waveforms of opportunity for passive radar application, a suboptimal batching strategy is usually employed to contain the computational load required for the evaluation of the cross-ambiguity function (e.g., see [1, 9]). Particularly, the reference and surveillance signals are fragmented into batches which are first separately range compressed and then jointly processed via a bank of Doppler filters. This allows emulating the fast-time/slow-time framework typical of a pulsed radar. We denote with M the number of batches, or pulses, in each CPI and with T the batch duration, which also corresponds to the equivalent pulse repetition time.

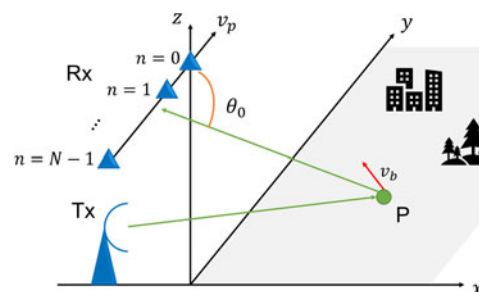


Figure 1. A sketch of the adopted system geometry.

We assume that the observed scene is characterized by both stationary scatterers and moving targets, and we denote with θ_0 the angle between the array end-fire and the receiver to scatterer line of sight. As known, the stationary scatterers contribute to the overall clutter return, which may hide the echoes from potential moving targets of interest.

Our aim is to exploit the described receiving-only system to detect slow-moving targets against clutter and noise. In the following, we will consider three simplifying assumptions, referred to as hypotheses H_1 , H_2 , and H_3 for future reference.

Hypothesis 1 (H_1): High clutter-to-noise power ratio (CNR). First, we will assume high CNR conditions. This is relatively common condition when dealing with mobile passive radars for short- and medium-range applications, for which the performance is usually clutter limited.

Hypothesis 2 (H_2): Perfect DPCA condition. As is well known, the DPCA techniques require the PRF to be synchronized with the platform velocity so that the n th antenna occupies the position of the $(n - 1)$ th after an integer number K_n of pulses. This is known as perfect DPCA condition. Denoting with ΔT_n the time interval required for the n th antenna to occupy the position of the $(n - 1)$ th, we have

$$\Delta T_n = \frac{d_n - d_{n-1}}{v_p} \tag{2}$$

Therefore, the perfect DPCA condition is satisfied if each of the time intervals ΔT_n in equation (2) is an integer multiple of the batch duration, namely,

$$\begin{aligned} \Delta T_n &= \frac{d_n - d_{n-1}}{v_p} = K_n \cdot T, \\ K_n &\in \mathbb{N}, n = 1, \dots, N - 1. \end{aligned} \tag{3}$$

The implications of equation (3) are clearly visible in Fig. 2, which shows the positions consecutively occupied by the $N = 3$ antenna elements in different time instants. Denoting with p the index of a generic position, we note that each antenna takes the p th position in an instant corresponding to the starting time of one of the M pulses. For now, we only consider uniform spacings between the sensors (i.e., $d_n - d_{n-1} = d, \forall n$), so that all the delays ΔT_n are equal (i.e., $\Delta T_n = K_n \cdot T = K \cdot T, \forall n$). In Fig. 2, we assumed $K = 2$.

In the reminder of this paper, we assume that the perfect DPCA condition is always satisfied, meaning that the array inter-element distances, the platform velocity, and the batch duration are constrained through equation (3). Note that satisfying this condition is relatively straightforward when CW signals are fragmented into batches. As a matter of fact, in such cases, the equivalent PRF corresponds to the inverse of the batch duration and can be chosen so as to satisfy equation (3).

Hypothesis 3 (H_3): Absence of internal clutter motion (ICM). In the following, we will assume the absence of ICM, meaning that the clutter scatterers have no (or negligible) intrinsic radial velocity. On the one hand, this hypothesis allows guaranteeing that the Doppler shift of an echo from a stationary scatterer only depends on the platform motion and can thus be univocally determined if the direction of arrival of the scatterer is known. On the other hand, the absence of ICM allows guaranteeing that the clutter returns do

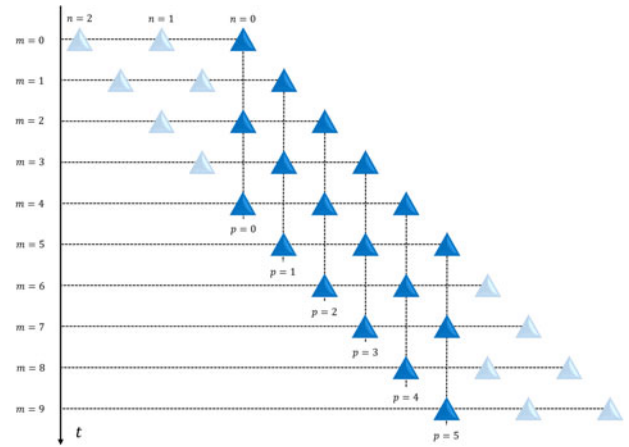


Figure 2. The set of positions consequently occupied by different antenna elements in different time instants. The ULA configuration $\mathbf{z} = [0.0.5.1.0] \lambda$ has been used. We assumed $K = 2$. The perfect DPCA condition guarantees perfect alignment between the N antennas.

not fluctuate from pulse to pulse so that different antenna elements occupying a given position at different times will observe exactly the same stationary scene.

Signal model

Let \mathbf{x} denote the space-time data vector relative to the l th range bin. This vector can be written as the sum of three contributions:

$$\mathbf{x} = \mathbf{t} + \mathbf{c} + \mathbf{n}. \tag{4}$$

Particularly, \mathbf{t} is a space-time column vector collecting the echoes from the moving target, \mathbf{c} is a column vector collecting the returns from the stationary scatterers located at the l th range bin, and \mathbf{n} is a column vector collecting additive white Gaussian noise samples. We also denote with $\mathbf{d} = \mathbf{c} + \mathbf{n}$ the overall disturbance signal.

In the following, we resort to the data selection strategy adopted in the studies by Lombardo [21] and Lombardo et al. [22], which is designed to remove the CPI border effect due to sensor misalignments. The idea is to only integrate the pulses collected from the positions sequentially occupied by each of the N sensors. This corresponds to discarding the first and the last pulses received by the antenna elements at the borders of the array. Denoting with P the total number of positions sequentially occupied, the position index $p = 0, \dots, P - 1$ can be written in terms of the space and time indices, n and m , respectively, as follows:

$$p = m - \frac{d_n}{v_p T}. \tag{5}$$

Figure 2 shows a graphical representation of the described data selection strategy. The discarded pulses are colored in light blue, while the ones used for integration are colored in dark blue. If the perfect DPCA condition is satisfied, this strategy allows guaranteeing that the integrated pulses are received by the N antennas from the same set of P positions.

Based on the adopted selection strategy, the data vector \mathbf{x} ($NP \times 1$) in equation (4), which collects the observations of the N antennas from the P positions, can be written as follows:

$$\mathbf{x} = \left[\mathbf{x}_0 \quad \mathbf{x}_1 \quad \dots \quad \mathbf{x}_{P-1} \right]^T \tag{6}$$

where \mathbf{x}_p ($p = 0, \dots, P - 1$) is an $(N \times 1)$ column vector collecting the pulses received by the N antennas from the p th position.

Based on the aforementioned data selection and assuming a perfect DPCA condition (H_2), the target contribution \mathbf{t} in equation (4) can be written as follows:

$$\mathbf{t} = \mathbf{s}_{pos}(\theta_0, \nu_b) \otimes \mathbf{s}_a(\nu_b) \quad (7)$$

where

- “ \otimes ” denotes the Kronecker product;
- the vector $\mathbf{s}_{pos}(\theta_0, \nu_b)$ ($P \times 1$) collects the P spatial phase shifts between the p th position and the first one

$$\mathbf{s}_{pos}(f_d) = \{\exp(j2\pi f_d(\theta_0, \nu_b)pT)\}_{p=0\dots P-1}, \quad (8)$$

with θ_0 being the target direction of arrival and $f_d(\theta_0, \nu_b)$ being the bistatic Doppler frequency of the considered target. In turn, the Doppler frequency can be decomposed into two contributions:

$$f_d = \frac{\nu_p \cos \theta_0}{\lambda} - \frac{\nu_b}{\lambda}, \quad (9)$$

where $\nu_p \cos \theta_0$ is the radial component of the platform velocity and ν_b is the intrinsic radial component of the observed target;

- the vector $\mathbf{s}_a(\nu_b)$ ($N \times 1$) collects the amplitudes and phases of the target’s echo at the N antennas from the generic position and depends on the propagation loss, the array layout, and the target velocity. In “Nonadaptive multichannel DPCA”, we will consider different models for vector $\mathbf{s}_a(\nu_b)$ depending on the assumptions made on the observed target, and this will allow us to derive different detection schemes.

The disturbance components \mathbf{c} ($NP \times 1$) and \mathbf{n} ($NP \times 1$) are modeled as statistically independent Gaussian random variables with zero mean and covariance matrices \mathbf{Q}_c and \mathbf{Q}_n , respectively. Specifically, the covariance matrix for thermal noise is simply written as $\mathbf{Q}_n = \sigma_n^2 \mathbf{I}_{NP}$, where $\sigma_n^2 = \frac{1}{NP} E\{\mathbf{n}^H \mathbf{n}\}$ is the noise power level at the generic antenna element, and we assumed identical receiving channels.

To derive a closed-form expression for the CCM \mathbf{Q}_c , we proceed as follows. First, note that the overall clutter return c from the l th range cell can be modeled as the superposition of the clutter returns from the stationary scatterers located in the angular sector $\Theta = [-\pi, \pi]$:

$$\mathbf{c} = \int_{-\pi}^{\pi} A_c(\theta) \mathbf{s}(\theta, \nu_b) d\theta \quad (10)$$

where $A_c(\theta)$ is the complex amplitude of the return from the stationary scatterer located at the l th range bin and at angle θ and $\mathbf{s}(\theta)$ is the corresponding space–time steering vector that can be written as follows:

$$\mathbf{s}(\theta) = \mathbf{s}_{pos}(\theta, 0) \otimes [1, 1, \dots, 1]^T \quad (11)$$

since, dealing with the stationary scene ($\nu_b = 0$) and having assumed the absence of ICM (H_3), the clutter echoes collected by the N antennas from a given position p are identical.

By defining $\mathbf{1}_N = [1, 1, \dots, 1]^T$, the expression of the CCM \mathbf{Q}_c can be developed as follows:

$$\begin{aligned} \mathbf{Q}_c &= E\{\mathbf{c}\mathbf{c}^H\} = \\ &= \int_{-\pi}^{\pi} \int_{-\pi}^{\pi} E\{A_c(\theta) A_c^*(\theta')\} \mathbf{s}(\theta) \mathbf{s}^H(\theta') d\theta d\theta' = \\ &= \int_{-\pi}^{\pi} \sigma_c^2(\theta) (\mathbf{s}_{pos}(\theta, 0) \otimes \mathbf{1}_N) (\mathbf{s}_{pos}^H(\theta, 0) \otimes \mathbf{1}_N) d\theta \end{aligned} \quad (12)$$

where we assumed that the amplitudes of the returns from different scatterers are independent, i.e.,

$$E\{A_c(\theta) A_c^*(\theta')\} = \begin{cases} 0, & \text{for } \theta \neq \theta' \\ \sigma_c^2(\theta), & \text{for } \theta = \theta'. \end{cases} \quad (13)$$

Eventually, we obtain

$$\begin{aligned} \mathbf{Q}_c &= \int_{-\pi}^{\pi} \sigma_c^2(\theta) [\mathbf{s}_{pos}(\theta, 0) \mathbf{s}_{pos}^H(\theta, 0)] d\theta \otimes [\mathbf{1}_N \mathbf{1}_N^H] = \\ &= \mathbf{K}_P \otimes \mathbf{K}_N. \end{aligned} \quad (14)$$

In the last expression of equation (14), we successfully decoupled the spatial and the temporal components of the CCM. Specifically, $\mathbf{K}_P = \int_{-\pi}^{\pi} \sigma_c^2(\theta) [\mathbf{s}_{pos}(\theta, 0) \mathbf{s}_{pos}^H(\theta, 0)] d\theta$ is a $P \times P$ cross-correlation matrix of the clutter returns observed by a fixed antenna from the P positions, while $\mathbf{K}_N = [\mathbf{1}_N \mathbf{1}_N^H]$ is a rank-one $N \times N$ cross-correlation matrix of the clutter returns observed by the N antennas from a fixed position, which are perfectly correlated due to the adopted H_2 and H_3 hypotheses.

Hence, the overall disturbance covariance matrix (DCM) can be written as follows:

$$\mathbf{Q} = \sigma_n^2 \mathbf{I}_{NP} + \mathbf{Q}_c. \quad (15)$$

Finally, by recalling the following matrix inversion lemma:

$$\mathbf{B} = \mathbf{A} + \mathbf{U}\mathbf{V}$$

$$\mathbf{B}^{-1} = \mathbf{A}^{-1} - \mathbf{A}^{-1}\mathbf{U}(\mathbf{I} + \mathbf{V}\mathbf{A}^{-1}\mathbf{U})^{-1}\mathbf{V}\mathbf{A}^{-1} \quad (16)$$

we obtain a closed-form expression also for the inverse DCM:

$$\mathbf{Q}^{-1} = \frac{1}{\sigma_n^2} \{\mathbf{I}_{NP} - ([\sigma_n^2 \mathbf{K}_P^{-1} + \mathbf{N}\mathbf{I}_P]^{-1} \otimes [\mathbf{1}_N \mathbf{1}_N^H])\}. \quad (17)$$

Under the hypothesis H_1 of high CNR, we have $\sigma_n^2 \mathbf{K}_P^{-1} \rightarrow 0$ as $\text{CNR} \rightarrow +\infty$, and the inverse DCM expression in equation (17) further simplifies into

$$\begin{aligned} \mathbf{Q}^{-1} &= \frac{1}{\sigma_n^2} \left\{ \mathbf{I}_{NP} - \left(\mathbf{I}_P \otimes \frac{1}{N} [\mathbf{1}_N \mathbf{1}_N^H] \right) \right\} = \\ &= \frac{1}{\sigma_n^2} \left\{ \mathbf{I}_P \otimes \left(\mathbf{I}_N - \frac{1}{N} [\mathbf{1}_N \mathbf{1}_N^H] \right) \right\} = \frac{1}{\sigma_n^2} \{\mathbf{I}_P \otimes \mathbf{\Pi}_N\}. \end{aligned} \quad (18)$$

where $\mathbf{\Pi}_N = \left(\mathbf{I}_N - \frac{1}{N} [\mathbf{1}_N \mathbf{1}_N^H] \right)$. Of course, \mathbf{Q}^{-1} is a tight approximation of the true DCM only if the hypotheses H_1 – H_3 are satisfied.

Nonadaptive multichannel DPCA detectors

To derive the optimal detector based on the assumed signal model, we resort to the likelihood ratio test (LRT):

$$L(\mathbf{x}) = \frac{e^{(\mathbf{x}-\mathbf{t})^H \mathbf{Q}^{-1}(\mathbf{x}-\mathbf{t})}}{e^{\mathbf{x}^H \mathbf{Q}^{-1} \mathbf{x}}} \geq \gamma, \quad (19)$$

where γ is an appropriate threshold. By evaluating the log-likelihood $\Lambda(\mathbf{x}) = \log(L(\mathbf{x}))$, we obtain

$$\Lambda(\mathbf{x}) = -\mathbf{x}^H \mathbf{Q}^{-1} \mathbf{t} - \mathbf{t}^H \mathbf{Q}^{-1} \mathbf{x} + \mathbf{t}^H \mathbf{Q}^{-1} \mathbf{t}. \quad (20)$$

Substituting equations (7) and (18) in equation (20) and omitting the dependence of the target component \mathbf{t} on θ_0 and v_b for ease of notation, we obtain

$$\begin{aligned} \Lambda(\mathbf{x}) = & -\mathbf{x}^H \frac{1}{\sigma_n^2} (\mathbf{I}_P \otimes \mathbf{\Pi}_N) (\mathbf{s}_{pos} \otimes \mathbf{s}_a) \\ & - (\mathbf{s}_{pos}^H \otimes \mathbf{s}_a^H) \frac{1}{\sigma_n^2} (\mathbf{I}_P \otimes \mathbf{\Pi}_N) \mathbf{x} \\ & + (\mathbf{s}_{pos}^H \otimes \mathbf{s}_a^H) \frac{1}{\sigma_n^2} (\mathbf{I}_P \otimes \mathbf{\Pi}_N) (\mathbf{s}_{pos} \otimes \mathbf{s}_a). \end{aligned} \quad (21)$$

Defining the $(N \times 1)$ column vector $\boldsymbol{\chi} = \{\mathbf{s}_{pos}^H \otimes \mathbf{I}_N\} \mathbf{x}$, we can rewrite equation (21) as follows:

$$\Lambda(\mathbf{x}) = -\frac{1}{\sigma_n^2} \boldsymbol{\chi}^H \mathbf{\Pi}_N \mathbf{s}_a - \frac{1}{\sigma_n^2} \mathbf{s}_a^H \mathbf{\Pi}_N \boldsymbol{\chi} + P \mathbf{s}_a^H \mathbf{\Pi}_N \mathbf{s}_a. \quad (22)$$

Note that $\boldsymbol{\chi}$ represents the Doppler bin of the DFT (discrete Fourier transform) of \mathbf{x} , corresponding to the Doppler frequency f_d for which the target is sought. Finally, defining the column vector \mathbf{y} ($N \times 1$) as

$$\mathbf{y} = \frac{1}{\sigma_n^2} \mathbf{\Pi}_N \boldsymbol{\chi}, \quad (23)$$

the log-likelihood in equation (22) can be rewritten as follows:

$$\Lambda(\mathbf{x}) = -\mathbf{y}^H \mathbf{s}_a - \mathbf{s}_a^H \mathbf{y} + P \mathbf{s}_a^H \mathbf{\Pi}_N \mathbf{s}_a. \quad (24)$$

Note that each element of \mathbf{y} can be interpreted as the output of a multichannel DPCA. To show this, let us rewrite equation (23) for the case of $N = 2$ antennas:

$$\mathbf{y} = \frac{1}{\sigma_n^2} \frac{1}{2} \begin{bmatrix} 1 & -1 \\ -1 & 1 \end{bmatrix} \begin{bmatrix} \chi[0] \\ \chi[1] \end{bmatrix} = \frac{1}{2\sigma_n^2} \begin{bmatrix} \chi[0] - \chi[1] \\ -\chi[0] + \chi[1] \end{bmatrix}. \quad (25)$$

As apparent, \mathbf{y} collects two equal and opposite values, corresponding to the output of a conventional DPCA. In turn, the rows of $\mathbf{\Pi}_{N=2}$ contain the two possible permutations of the weights of a standard single canceler [23], namely $\mathbf{v} = [1, -1]$. In other words, conventional DPCA can be seen as the counterpart of the single canceler for moving radar systems. While DPCA virtually compensates for the platform motion by subtracting the signals received by the two antennas at the time instants in which their phase centers occupy the same positions, a single canceler takes the difference between two temporally displaced replicas of the received signal, resorting to a tapped delay line (TDL) with $N = 2$ taps and weight coefficients $\mathbf{v} = [1, -1]$. In either case, the clutter returns from stationary scatterers cancel out, while the echoes from moving targets, shifted in phase due to their own radial motion, are preserved.

In general, for $N \geq 2$, the n th element of \mathbf{y} is a linear combination of the N elements of $\boldsymbol{\chi}$, with coefficients given by the n th row of $\mathbf{\Pi}_N$. Particularly, each row of $\mathbf{\Pi}_N$ contains one of the N permutations of the weights in the vector $\mathbf{v} = \left[\frac{N-1}{N}, -\frac{1}{N} \mathbf{1}_{N-1} \right]$. Note that the vector \mathbf{v} is such that

$$\sum_{i=1}^N v[i] = 0. \quad (26)$$

This is a fundamental property of the weights of any TDL-based clutter canceler, which guarantees that the filter response will show a notch at zero bistatic velocity, enabling the suppression of the

clutter component. Incidentally, we note that the specific order in which the weights are applied does not affect clutter cancellation capabilities, while it may affect the target response, depending on its radial velocity.

Based on the foregoing considerations and observing that the log-likelihood function in equation (24) depends on unknown parameters, we resort to the generalized LRT, in which the log-likelihood is maximized with respect to the unknowns. Depending on the model adopted for the target contribution, this approach allows us to derive a series of nonadaptive multichannel DPCA-like detectors suitable for low-cost radar systems.

Fully coherent detector

To derive this first detector, we assume that the target contribution in equation (7) is determined up to a multiplicative constant given by the deterministic but unknown complex target amplitude A , i.e., $\mathbf{s}_a = A \mathbf{s}_{del}$, where

$$\mathbf{s}_{del}(v_b) = \left\{ \exp \left(j \frac{2\pi v_b d_n}{\lambda v_p} \right) \right\}_{n=0, \dots, N-1}. \quad (27)$$

is fully specified and depends on the antenna element spacings d_n and on the ratio v_b/v_p between the target bistatic velocity and the platform velocity.

In this case, maximizing equation (24) with respect to the unknown parameter A , we have

$$\max_A \{\Lambda\} = -\mathbf{y}^H \tilde{A} \mathbf{s}_{del} - \tilde{A}^* \mathbf{s}_{del}^H \mathbf{y} + P \tilde{A}^* \mathbf{s}_{del}^H \mathbf{\Pi}_N \tilde{A} \mathbf{s}_{del}, \quad (28)$$

which is maximum for $\tilde{A} = \frac{\mathbf{s}_{del}^H \mathbf{y}}{P \mathbf{s}_{del}^H \mathbf{\Pi}_N \mathbf{s}_{del}}$, yielding

$$\max_A \{\Lambda\} = \frac{|\mathbf{s}_{del}^H \mathbf{y}|^2}{P \mathbf{s}_{del}^H \mathbf{\Pi}_N \mathbf{s}_{del}}. \quad (29)$$

By selecting an appropriate threshold value T to guarantee the desired false alarm probability, we obtain the following detector:

$$|\mathbf{s}_{del}^H \mathbf{y}|^2 \geq T, \quad (30)$$

where the denominator of equation (29) has been included in the threshold T , being a constant value. In the following, this will be referred to as fully coherent (FC) detector as both the spatial and the temporal phase information are exploited.

Based on equations (23), (27), and (30), the FC detector can be interpreted as the cascade of the following operations:

1. Coherent integration along the position domain by evaluating DFT of the data vector \mathbf{x} .
2. Suppression of the clutter contributions within the generic Doppler bin $\boldsymbol{\chi}$ of the Fourier-transformed data vector by evaluating $\mathbf{y} = \frac{1}{\sigma_n^2} \mathbf{\Pi}_N \boldsymbol{\chi}$.
3. Coherent integration along the antenna domain by multiplying \mathbf{y} by the temporal steering vector $\mathbf{s}_{del}^H(v_b)$.

Based on the observations at the end of the previous section, the FC detector can also be interpreted as the coherent integration along the antenna domain of the different outputs of N multichannel DPCAs, collected in the vector \mathbf{y} , each obtained considering a different permutation of the weights \mathbf{v} in the n th row of $\mathbf{\Pi}_N$.

To assess the target detection performance of the FC detector, we define the signal-to-clutter-plus-noise power ratio (SCNR)

as follows:

$$SCNR_{FC} = \frac{P_s^{out}}{P_d^{out}} = \frac{|\mathbf{w}_{FC}^H \mathbf{t}|^2}{E \left\{ |\mathbf{w}_{FC}^H \mathbf{d}|^2 \right\}} = \frac{A^2 |\mathbf{w}_{FC}^H (\mathbf{s}_{pos} \otimes \mathbf{s}_{del})|^2}{\mathbf{w}_{FC}^H \tilde{\mathbf{Q}} \mathbf{w}_{FC}} \quad (31)$$

where P_s^{out} is the output power of the useful signal, $P_d^{out} = \sigma_{c^{out}} + \sigma_n^{out}$ is the output power of the disturbance component, $\tilde{\mathbf{Q}} = E \left\{ \mathbf{d} \mathbf{d}^H \right\}$ denotes the true DCM, and \mathbf{w}_{FC} is an $(NP \times 1)$ column vector collecting the complex-valued coefficients, which represent the sequence of operations performed by the FC detector, namely,

$$\mathbf{w}_{FC} = \frac{1}{\sigma_n^2} \left\{ \mathbf{s}_{pos} \otimes \mathbf{I}_N \right\} \left(\mathbf{I}_N - \frac{1}{N} [\mathbf{1}_N \mathbf{1}_N^H] \right) \mathbf{s}_{del}. \quad (32)$$

Substituting the expression of \mathbf{w}_{FC} in equation (31), we obtain

$$SCNR_{FC} = \frac{|A|^2 NP}{\sigma_n^2} \left[1 - \left| \frac{1}{N} \sum_{n=0}^{N-1} \exp \left(j \frac{2\pi}{\lambda} \frac{v_b}{v_p} d_n \right) \right|^2 \right]. \quad (33)$$

Clearly, the last expression in equation (33) holds only when $\mathbf{Q} = \tilde{\mathbf{Q}}$, namely if hypotheses H_1 – H_3 are satisfied.

Assuming a Swerling 0 (SW0) model for the target amplitudes, we can evaluate the detection performance in terms of probability of false alarm (P_{fa}) and probability of detection (P_d), using the following well-known expressions:

$$P_{fa} = \exp \left(-\frac{T^2}{\sigma_N^2} \right) \quad (34)$$

$$P_d = Q \left(\sqrt{2 SCNR_{FC}}, \sqrt{2T^2} \right) \quad (35)$$

where T is the threshold value and $Q(a, b)$ is the Marcum function.

In conclusion, when H_1 – H_3 are satisfied, the FC detector achieves optimal performance without involving any estimation process. However, it requires both the steering vectors $\mathbf{s}_{pos}(\theta_0, v_b)$ and $\mathbf{s}_{del}(v_b)$ to be completely determined. Hence, implementing the FC detector involves a two-dimensional exhaustive search along the angle–velocity axes. In the following subsections, we introduce two additional detectors that do not rely on the phase information in $\mathbf{s}_{del}(v_b)$, thereby reducing the processing complexity.

Partially coherent detector

Note that the two-dimensional exhaustive search can be circumvented by performing noncoherent integration along the antenna domain. In fact, we observe that the steering vector $\mathbf{s}_{pos}(\theta_0, v_b)$ depends on both θ_0 and v_b . However, equation (8) shows that $\mathbf{s}_{pos}(\theta_0, v_b)$ actually depends only on the target Doppler frequency $f_d(\theta_0, v_b)$. Therefore, the phase information in $\mathbf{s}_{pos}(\theta_0, v_b)$ can be exploited by resorting to a bank of filters tuned to different Doppler frequencies. By neglecting the phase information in $\mathbf{s}_{del}(v_b)$, we only need a one-dimensional exhaustive search along the target Doppler frequency axis.

Based on this observation, in the following, we introduce the partially coherent (PC) detector, which only exploits the phase information along the position domain. Recalling that only a limited number of receiving channels should be used to preserve ease of deployment, the PC detector should not undergo significant losses compared to the FC one.

To derive the PC detector, we modify the model adopted in “System geometry and reference scenario” for \mathbf{s}_a to reflect the limited knowledge on the target velocity. To this purpose,

$\mathbf{s}_a = [A_0, \dots, A_{N-1}]$ is modeled as a vector of deterministic but unknown complex amplitudes. Maximizing equation (24) with respect to \mathbf{s}_a , we have

$$\max_{A_0, A_1, \dots, A_{N-1}} \left\{ -\mathbf{y}^H \mathbf{s}_a - \mathbf{s}_a^H \mathbf{y} + P \mathbf{s}_a^H \mathbf{\Pi}_N \mathbf{s}_a \right\} \quad (36)$$

whose maximum is given by

$$\max_{A_0, A_1, \dots, A_{N-1}} \{ \Lambda \} = \frac{1}{P} \mathbf{y}^H \mathbf{y}. \quad (37)$$

By selecting an appropriate threshold value T to guarantee the desired false alarm probability, we obtain the following detector:

$$|\mathbf{y}|^2 \geq T \quad (38)$$

where P has been included in the threshold T .

Since the PC detector involves nonlinear operations, its performance cannot be evaluated in terms of the SCNR, as the superposition principle does not hold, and the effects of the different signal components cannot be analyzed separately. Therefore, we directly report the expressions for the achieved P_{fa} and the P_d :

$$P_{fa} = \frac{1}{(N-2)!} \gamma \left(\frac{(N-1)T}{N\sigma_N^2}, N-1 \right) \quad (39)$$

$$P_d = Q \left(\sqrt{\frac{(N-1)2\xi}{N\sigma_N^2}}, \sqrt{\frac{(N-1)2T^2}{N\sigma_N^2}}, N-1 \right) \quad (40)$$

where $\gamma \left(\frac{T}{\alpha}, N-1 \right)$ is the upper incomplete gamma function, T is the threshold value, $\alpha = \frac{N-1}{N}$ is a scale factor, and ξ is a parameter depending on the input power of the target signal. The detailed derivation of these expressions can be found in Appendix A.

Apodized partially coherent detector

Based on the foregoing considerations, the apodization approach introduced in the study by Quirini et al. [11] appears to be a sub-optimal variant of the PC detector. Therein, the maximum between the absolute square values of the N DPCA outputs collected in \mathbf{y} was evaluated, thus obtaining

$$\max(\mathbf{y}^* \odot \mathbf{y}) \geq T, \quad (41)$$

where \odot denotes the element-wise product. In the following, this detector will be referred to as apodization partially coherent (APC) detector.

As for the PC detector, the performance of the APC detector is evaluated in terms of P_{fa} and P_d . In this case, we have we have the following upper bounds for the false alarm and detection probabilities:

$$P_{fa} \lesssim 1 - \left(1 - e^{-T/\sigma_N^2} \right)^N \quad (42)$$

$$P_d < 1 - \prod_{k=0}^{N-1} \left(1 - Q \left(\sqrt{\frac{2(\mu_k^R + \mu_k^I)}{\sigma_N^2}}, \sqrt{\frac{2T}{\sigma_N^2}} \right) \right). \quad (43)$$

The detailed derivation of these expressions can be found in Appendix B.

Performance evaluation and comparison

In this final subsection, we validate the theoretical characterization of the performance of the FC, PC, and APC detectors via numerical analysis. To this end, the simulations are carried out assuming the

validity of the hypotheses H_1-H_3 and generating the signal components according to the model outlined in “System geometry and signal model”. Hence, in this simulation, the conditions in which the three detectors have been defined are always satisfied. By ensuring this, we can effectively validate the theoretical performance of these detectors.

To this aim, for now we consider a phased array radar receiver $\mathbf{z} = [0.5 \ 1.0] \lambda$ with $N = 3$ antenna elements, characterized by uniform spacings of $\lambda/2$ between the sensors. We also assume that $P = 6$ positions are coherently integrated. Furthermore, we assume that the platform velocity v_p is chosen so that the n th antenna occupies the position of the $n - 1$ th after $K = 2$ pulses. With this choice of parameters, we precisely match the conditions sketched in Fig. 2. We also assume that the input signal-to-noise power ratio (SNR), defined as the ratio between the absolute square of complex target amplitude $|A|^2$ and the input noise power σ_n^2 , is equal to $SNR_{in} = 0dB$.

The validity of the P_{fa} and P_d expressions shown in the previous subsection is verified by means of a Monte Carlo simulation with $R_{MC} = 10^6$ runs. Specifically, the useful component of the received signal is generated as in equation (4), the noise component is modeled as a complex white Gaussian random variable, and the clutter component is modeled as a complex Gaussian random variable with covariance matrix \mathbf{Q}_c as in equation (14). The sum of these contributions corresponds to an $(NP \times 1)$ column vector \mathbf{x} , which is the simulated data vector relative to the l th range bin. The decision variable can be obtained from the data vector \mathbf{x} by using one of the three detectors defined in the previous subsections, namely the FC detector, the PC detector, or the APC detector.

First, we verify the derived P_{fa} expressions by evaluating the theoretical and simulated values of P_{fa} as a function of the threshold value, as shown in Fig. 3. As visible, all the derived theoretical expressions for P_{fa} , represented as solid curves, provide an accurate prediction of the simulated P_{fa} values, represented as colored markers. Specifically, the upper bound derived for the P_{fa} of the APC detector represents a good approximation for the actual P_{fa} value.

The simulated value for the P_d can be estimated as the ratio between the values of γ overcoming the threshold value T and the total number of Monte Carlo runs. For each detector, the threshold

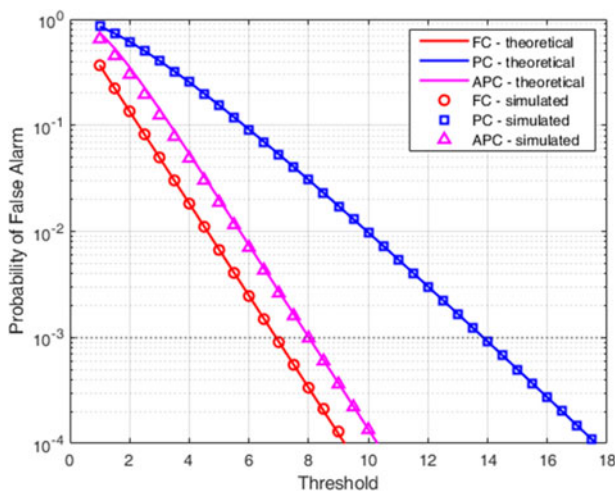


Figure 3. Probability of false alarm achieved by the FC, PC, and APC detectors, as a function of the threshold value.

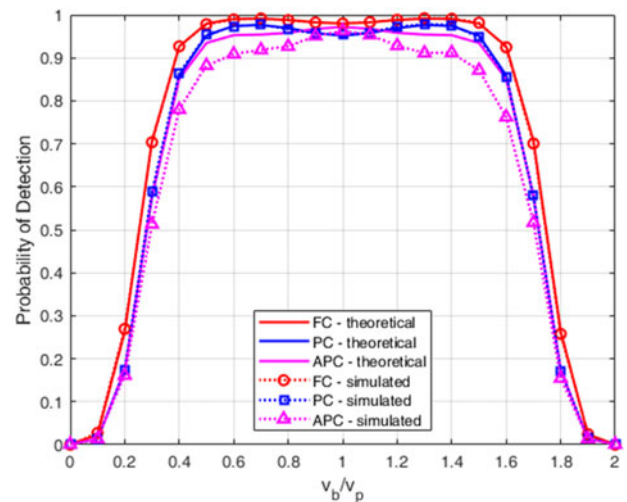


Figure 4. Probability of detection achieved by the FC, PC, and APC detectors, as a function of the ratio between target bistatic velocity v_b and the platform velocity v_p .

value T is determined by inverting the relative P_{fa} formula, namely equations (34), (39), and (42), respectively. In this case, a constant false alarm probability of $P_{fa} = 10^{-3}$ has been assumed.

The theoretical and simulated values of P_d are studied as a function of the ratio v_b/v_p between the target bistatic velocity and the platform velocity. The P_d values achieved by the different detectors are compared in Fig. 4. The red curve represents the FC detector, while the blue and the magenta ones represent the PC and the APC detectors, respectively. Furthermore, the solid lines represent the theoretical P_d values, while the markers represent the simulated ones. The following observations are in order:

- Since the clutter signal has been generated according to the CCM model in equation (14), no model mismatches can possibly be present. Therefore, the FC detector achieves optimal performance, thus providing a useful reference for the other detectors.
- The PC and the APC detectors achieve slightly degraded performances compared to the FC detector, due to the noncoherent integration along the antenna domain.
- Overall, the PC detector achieves higher P_d values than the APC one. This is visible by comparing not only the simulated values for P_d but also the theoretical prediction of the PC with the upper bound of the APC.
- Each of the three detectors shows a cancellation notch at $v_b = 0$, which enables clutter cancellation. This notch is also responsible for the partial attenuation affecting slow-moving targets.
- For the considered set of parameters, the cancellation notch shows replicas located at $\frac{v_b}{v_p} = 2k$, $k \in \mathbb{Z}$, which in turn result in the appearance of blind velocities. As discussed in the next section, the width of the cancellation notch and the distance between blind velocities depend on the array design.

In conclusion, both PC and APC detectors suffer from the non-coherent integration in the antenna domain, reaching lower P_d values compared to the FC detector. However, as mentioned earlier, these detectors do not require a two-dimensional exhaustive search on the bistatic target velocity v_b and on the target direction of arrival θ_0 , possibly making them an attractive alternative when designing a low-cost mobile passive radar.

To conclude this section, we note that improved detection performance on slow-moving targets could be achieved by limiting the notch width, and that the set of unambiguous target velocities could be widened by increasing the distance between consecutive notch ambiguous replicas. As shown in the next section, these two competing needs sensibly depend on the receiving array design. When an ULA configuration is used, improved performance can be achieved only by increasing the number of sensors. This is not always feasible when striving for cost-containment, weightlessness, and compactness. Therefore, in the next section, we explore the use of NULA configurations, with the aim of realizing satisfactory trade-offs between the width of the cancellation notch and the distance between blind velocities, all without increasing the number of sensors.

NULA configurations

As mentioned at the end of the last section, target detection performance depends not only on the detector used but also on the array configuration adopted as radar receiver. Therefore, alongside the implementation of appropriate processing techniques, it is essential to pay careful attention to the design of the receiving array, which is crucial to preserve ease of deployment and compactness.

When designing a receiving array configuration, two competing needs should be considered:

1. On the one hand, the global array length should be maximized. As a matter of fact, from Fig. 2, it is apparent that the global array length is directly related to the total observation time from the p th position. Maximizing the observation time results in an increased capability of distinguishing slow-moving targets from stationary scatterers, since the phase shift induced by the nonzero bistatic radial velocity of a slow-moving target is observed over a larger time span, ultimately resulting in a narrower cancellation notch.
2. On the other hand, the inter-element distances should be minimized. As a matter of fact, reducing the distance between the sensors corresponds to minimizing the delay between the observations from the p th position. This results in a finer sampling grid in the time domain, which allows to increase the maximum unambiguous velocity, ultimately resulting in a larger distance between two replicas of the cancellation notch.

As apparent, when a ULA configuration is adopted, these requirements cannot be simultaneously pursued, unless a larger number of receiving elements is employed. However, when dealing with low-cost mobile radar systems, every additional sensor adversely affects the system compactness. Hence, our aim is to make the most of the limited number of available antennas by resorting to nonuniform sensor distributions. In contrast, as also studied in [11–13], NULA configurations allow reducing the notch width without simultaneously increasing the distance between the notch replicas, benefiting the overall detection performance.

As an illustrative example, we consider the NULA configuration $\mathbf{z} = [0.5 \ 1.5] \lambda$, with the same minimum element distance of 0.5λ of the reference ULA array considered in “Nonadaptive multichannel DPCA”, and a larger maximum distance of 1.5λ . The set of $P = 6$ positions consecutively occupied by the $N = 3$ antenna elements is sketched in Fig. 5. Having assumed nonuniform sensor spacings, the time delay between the n th and the $n - 1$ th sensors now depends on the antenna index n and is given as follows:

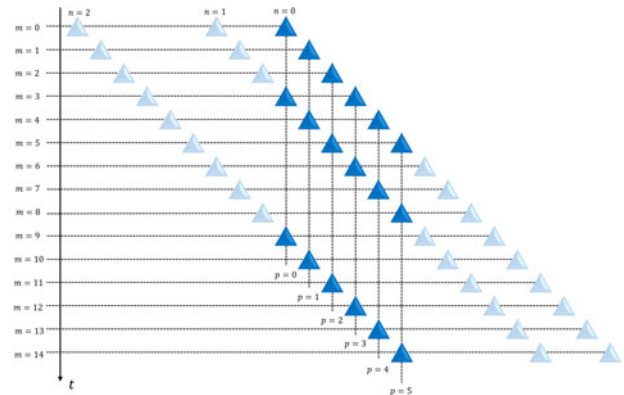


Figure 5. The set of positions consequently occupied by different antenna elements in different time instants. The NULA configuration $\mathbf{z} = [0.5 \ 1.5] \lambda$ has been used. We assumed $K_1 = 3$ and $K_2 = 6$. The perfect DPCA condition guarantees perfect alignment between the N antennas.

$$\Delta T_n = K_n \cdot T. \quad (44)$$

In Fig. 5 we assume $K_1 = 3$ and $K_2 = 6$. The positions outline clearly shows how the antenna design reflects in the time domain.

To better understand the role played by the inherent spatial diversity of NULA configurations, we note that each of the detectors introduced in the previous section represent a different way of combining the outputs of N different DPCA filters, each obtained considering one of the possible permutations of the weight vector $\mathbf{v} = \left[\frac{N-1}{N}, -\frac{1}{N} \mathbf{1}_{N-1} \right]$. Figure 6(a) and (b) shows these responses of the $N = 3$ DPCA filters (namely, absolute value of their outputs) as a function of the ratio v_b/v_p between the target bistatic velocity and the platform velocity obtained using the reference three-element ULA of “Nonadaptive multichannel DPCA” $\mathbf{z} = [0.5 \ 1.0] \lambda$ and the three-element NULA $\mathbf{z} = [0.5 \ 1.5] \lambda$, respectively.

Note that two of the three DPCA outputs in Fig. 6(a) are identical, due to the symmetry of the employed $\lambda/2$ -ULA configuration, while the all three DPCA outputs in Fig. 6(b) are different. This is a result of the spatial diversity characterizing the employed NULA configuration: one of the three outputs responds better to the targets with low v_b/v_p values, ultimately allowing to reduce the notch width, which is beneficial for the detection of slow-moving targets, while performing worse for the intermediate values; the other two outputs have a worse response to the targets with low v_b/v_p values, but a higher response at the intermediate results. Their combination allows to reduce the notch, without simultaneously changing the distance between the notch replicas, which are responsible for blind velocities.

To provide a wider analysis of the performance improvement achievable by jointly exploiting the detectors in “Nonadaptive multichannel DPCA” with the NULA configurations, we consider for the comparison also an ULA array with maximum element distance of 1.5λ and a NULA array with maximum element distance of λ but shorter minimum element distance. Therefore, we compare the theoretical and simulated performance of the three detectors derived in the previous section, operating with the four different array configurations:

1. The ULA $\mathbf{z}_1 = [0.50 \ 1.00] \lambda$.
2. The ULA $\mathbf{z}_2 = [0.75 \ 1.50] \lambda$.
3. The NULA $\mathbf{z}_3 = [0.35 \ 1.00] \lambda$.
4. The NULA $\mathbf{z}_4 = [0.50 \ 1.50] \lambda$.

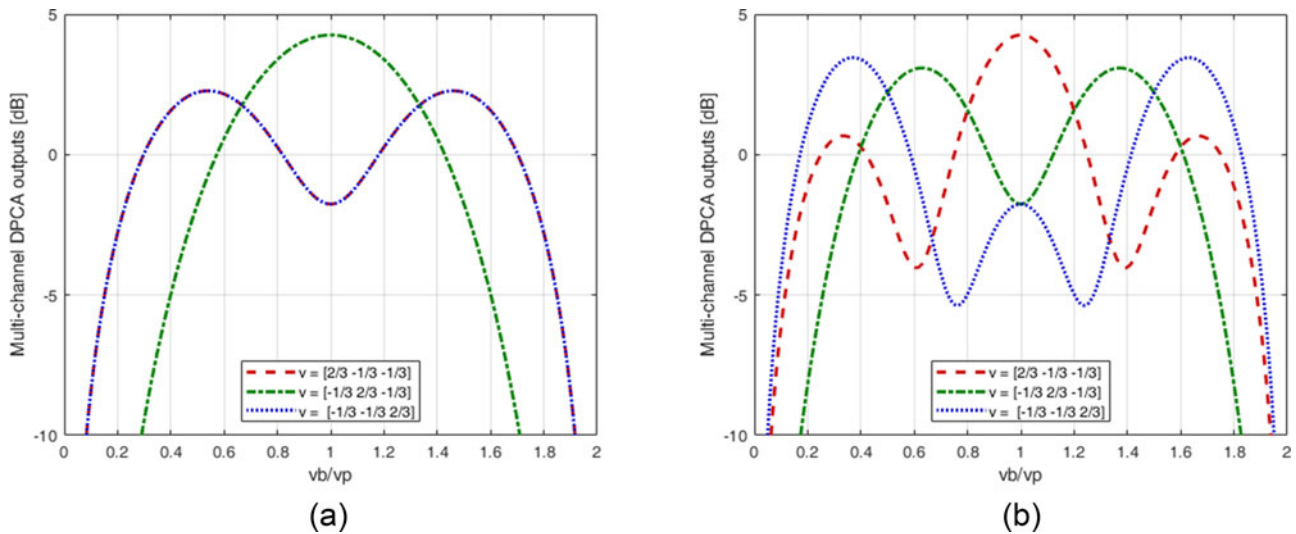


Figure 6. Outputs of $N = 3$ multichannel DPCAs, obtained using the weighting coefficients given by the N rows of $\mathbf{\Pi}_N$, and (a) the ULA $z = [0 \ 0.5 \ 1.0] \lambda$, (b) the NULA $z = [0 \ 0.5 \ 1.5] \lambda$.

A Monte Carlo simulation with $R_{MC} = 10^6$ runs is carried out as in “Nonadaptive multichannel DPCA”. A fixed false alarm probability of $P_{fa} = 10^{-3}$ has been assumed, and an estimate of the P_d value is obtained as the percentage of runs for which the threshold value T is overcome.

Figure 7(a–d) shows the results obtained by the three different detectors using the four different array configurations. The following observations are in order:

- As expected, an increased array total length results in a narrower cancellation notch. This is clearly visible by comparing longer array configurations (i.e., z_2 or z_4) to shorter ones (i.e., z_1 or z_3).
- As also expected, a reduced minimum inter-element distance results in a larger distance between the notch replicas. Thus, for example, since configuration z_3 has the minimum inter-element distance, it achieves the maximum distance between two adjacent notch replicas. Conversely, configuration z_2 has the largest minimum inter-element distance, which results in the greater distance between two adjacent notch replicas.
- Different trade-offs between the notch width and the distance between the blind velocities could be achieved by choosing the appropriate NULA design. This flexibility is paid in terms of P_d fluctuations for the target velocities outside the clutter cancellation notch.
- The correspondence between the theoretical and the simulated values of P_d confirms the validity of the analysis.
- The loss of the PC and APC detectors with respect to the FC one increases as the array deviates from the ULA configuration. Specifically, the PC performs almost as the FC when used together with an ULA. In contrast, when trying to leverage the NULA to either narrow the cancellation notch or increase the distance between notch replicas, the performance gap between the detection losses achieved by the PC and the FC significantly increases.

In conclusion, when aiming at increasing the unambiguous velocity sector, the NULA configuration $z_3 = [0 \ 0.35 \ 1.00] \lambda$ represents a better design choice with respect to the $\lambda/2$ -ULA $z_1 = [0 \ 0.50 \ 1.00] \lambda$, as it allows to increase the distance between the

adjacent notch replicas without compromising on the notch width. Conversely, when interested in the detection of particularly slow-moving targets, the NULA $z_4 = [0 \ 0.50 \ 1.50] \lambda$ represents a better design choice with respect to the $3\lambda/2$ -ULA $z_2 = [0 \ 0.75 \ 1.50] \lambda$, as it allows to narrow down the cancellation notch without reducing the unambiguous velocity sector. In this case, it is likely that the performance loss of the PC detector (still limited but greater than for the ULA case) is acceptable for a low-cost sensor. However, if this is not the case, it is apparent that this loss can be avoided by implementing the full 2D filter bank required by the FC detector at the expense of providing the sensor with the necessary increased computational capability. An alternative would be using an ULA with four elements ($[0 \ 0.50 \ 1.0 \ 1.50] \lambda$ or $[0 \ 0.33 \ 0.66 \ 1.00] \lambda$) with a PC detector. This would trade processing hardware for antenna elements with their respective receiving channels, with the corresponding costs, mass, volume, and power absorptions.

Case study: passive radar system based on DVB-T

In the previous section, we always assumed that the DCM model is an accurate representation of the true clutter statistics, since the clutter signal has always been generated according to the statistics described by the CCM model in equation (14). In this section, we try to validate the above observations in a different simulated scenario in which the clutter signal is generated as the superposition of the returns from a grid of stationary scatterers rather than as a colored Gaussian sequence. Indeed, the proposed detectors are tested against a simulated data set, employing the same ULA and NULA configurations considered in “NULA configurations”. Differently from “Nonadaptive multichannel DPCA”, the simulated analysis focuses on a real-world scenario. Specifically, we consider a multichannel DVB-T-based passive radar installed on a ground moving platform.

The simulation setup recalls the one presented in [9] and [10]. An 8k mode DVB-T waveform of opportunity is used as a reference signal. The guard interval is equal to $T_G = T_U/4$, such that the overall duration of the orthogonal frequency-division multiplexing (OFDM) symbol is $T_{OFDM} = T_U + T_G = 1120\mu s$, being $T_U = 896\mu s$. This results in a CPI of about 0.57s, corresponding

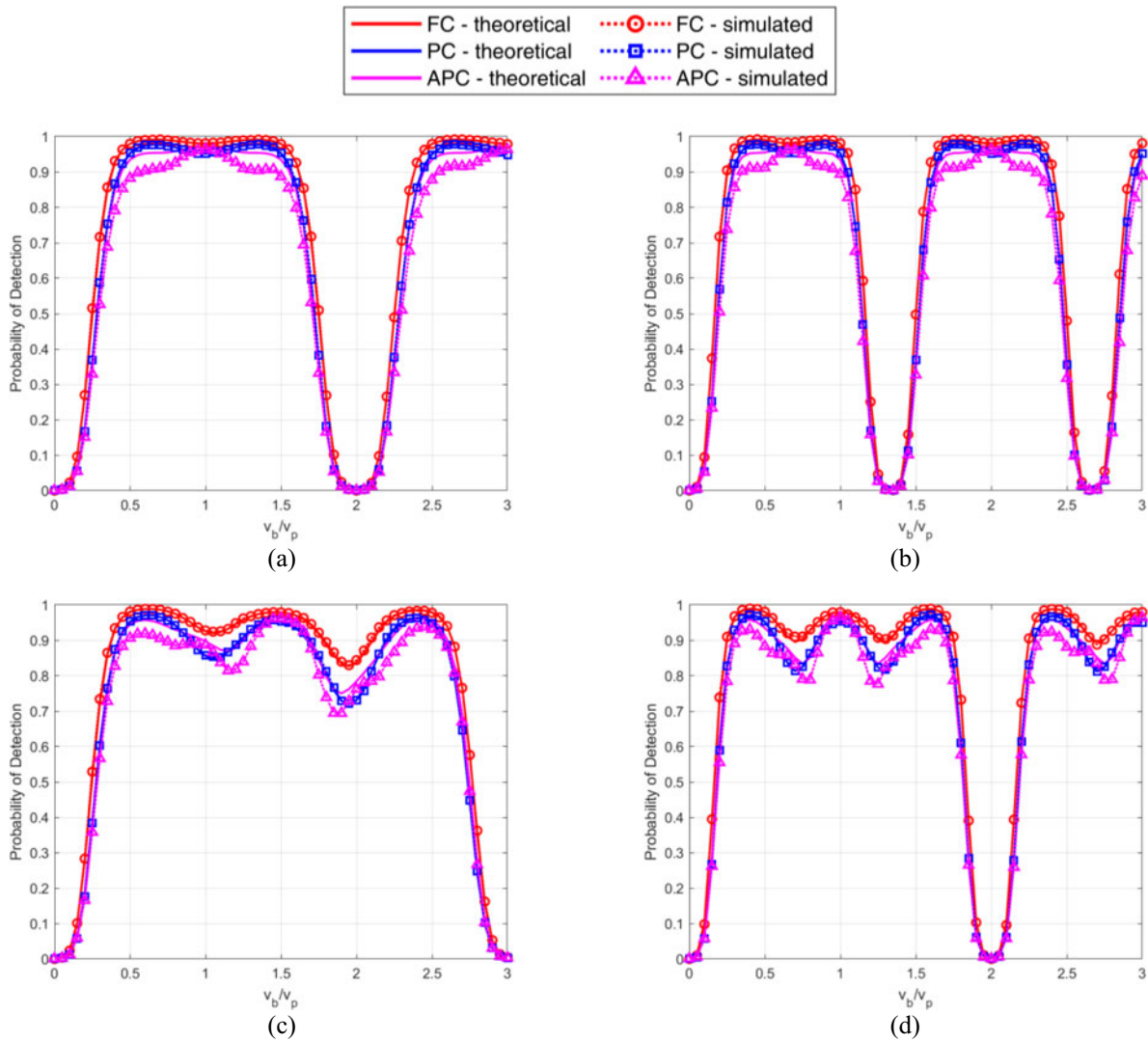


Figure 7. Probability of detection as a function of the ratio v_b/v_p for the three proposed detectors. (a) $z_1 = [0.0.50\ 1.00] \lambda$; (b) $z_2 = [0\ 0.75\ 1.50] \lambda$; (c) $z_3 = [0.0.35\ 1.00] \lambda$; (d) $z_4 = [0.0.50\ 1.50] \lambda$.

to 512 OFDM symbols. The carrier frequency has been set to $f_C = 690\text{MHz}$, which corresponds to the wavelength $\lambda \approx 0.4345\text{m}$. In this case, we assume that the reference signal is obtained by means of a decode/decode approach, so that a dedicated receiving channel for the reference signal is not needed.

The N receiving channels are installed on a ground moving platform. The platform velocity has been set to $v_p = 6.4655\text{m/s}$ so that the perfect DPCA condition holds for each of the arrays z_1, z_2, z_3 , and z_4 considered in the previous section. Specifically, for the chosen set of parameters, we have $\frac{\lambda}{v_p T} = 60$, i.e., the platform travels exactly one wavelength in 60 PRTs. This guarantees that the sub-wavelength inter-element distances in the chosen array configurations are also traveled in a time corresponding to integer multiple of PRTs.

As to the signal components, thermal noise has been generated as a zero mean, unitary variance, Gaussian-distributed complex random variable $\mathcal{N}(0, \sigma_N^2)$, and its power level has been deliberately set to unity (i.e., $\sigma_N^2 = 0\text{dB}$).

Table 1. Simulated targets parameters

	Bistatic radial velocity (v_b)	Bistatic range (R_b)	Direction of arrival (θ_t)
Target 1	1.5m/s	3.2km	90°
Target 2	-9m/s	1.9km	90°
Target 3	-13m/s	5.9km	90°
Target 4	16m/s	4.5km	90°

The four targets reported in Table 1 have been simulated:

The target signal is obtained as the superposition of the signals backscattered from these targets. Due to the unitary noise scaling, the overall input power $P_S^{(in)}$ also corresponds to the input SNR, for which we assumed $\text{SNR}_{in} = -55\text{dB}$.

Finally, a clutter scene spanning the first $R_b = 8\text{km}$, corresponding to $N_R = 1000$ range cell, and an angular sector $\Theta_q = [0, \pi]$, $\forall q$ has been simulated. The complex amplitudes of

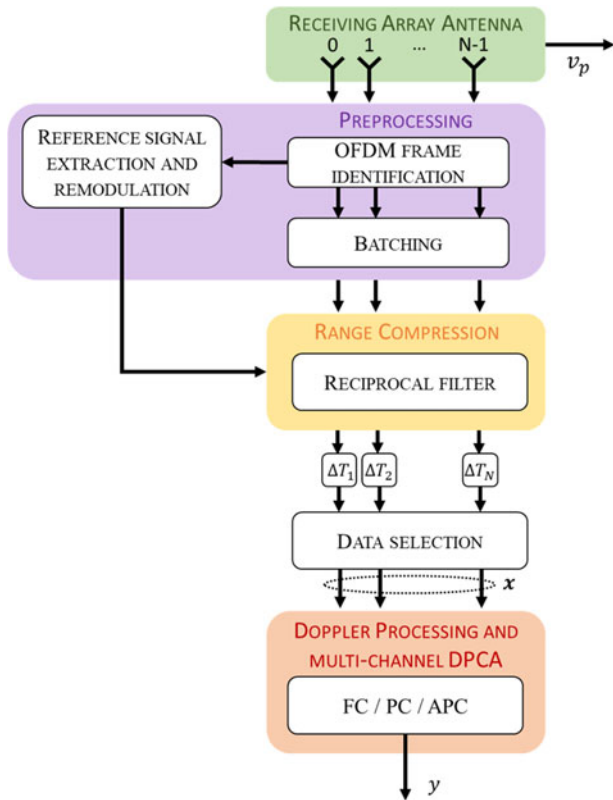


Figure 8. Sketch of the adopted processing scheme.

the scatterers are assumed to be independent and identically distributed, following a Gaussian probability density function. The absence of ICM is assumed. The clutter component is scaled in amplitude so that it has an assigned power level $P_C^{(in)}$ at the input of each receiving channel. Due to the unitary noise scaling, the input power level of the clutter component also corresponds to the input CNR, for which we assumed $CNR_{in} = 20\text{dB}$.

Figure 8 shows a sketch of the employed processing scheme, similar to the one described in [9]. First, a suboptimal batching strategy is adopted to contain the computational load required for the evaluation of the range-Doppler maps. Specifically, the CW signal is segmented into batches, which are separately range compressed and Doppler processed along the equivalent slow time dimension. The duration of one batch is assumed to be equal to the duration of one OFDM symbol, so that $T = T_{OFDM}$. As discussed in “System geometry and signal model”, the duration of one batch also corresponds to the equivalent PRT.

The subsequent range compression stage exploits a reciprocal filter in place of a matched filter. This allows to equalize the variability associated to the information content of the waveform of opportunity, which is fundamental to guarantee effective clutter cancelation, as extensively discussed in [9].

After range compression, the received signals are appropriately delayed by ΔT_n before applying the data selection strategy described in “System geometry and signal model”. This allows us to obtain the space-time data vector \mathbf{x} , which collects the returns from the N antenna from the P positions for the l th range bin.

Note that the data vector \mathbf{x} has not been generated according to the signal model in “System geometry and signal model”. However, assuming that the hypotheses H_1-H_3 still hold and that

the sidelobes of the exploited waveform of opportunity are properly controlled, the FC, PC, and APC detectors should still achieve satisfactory target detection performance.

Consequently, we proceed to evaluate the effectiveness of the proposed detectors in the described real-world scenario, with a specific focus on the PC detector. However, we note that similar considerations apply to the FC and APC detectors as well. As to the array design, we consider the same ULA and NULA configurations employed in the previous section.

To assess the detection performance of the PC detector for different array configurations, we report the achieved test statistics on the bistatic range-Doppler maps. Specifically, we define a series of desired P_{fa} values and we resort to equation (39) to evaluate the corresponding thresholds. Then, for each pixel in the map, we report the P_{fa} value that corresponds to the minimum threshold required for that pixel to yield a detection. The results are reported as $\log_{10} P_{fa}$.

The described range-Doppler maps are reported in Fig. 9. Specifically, Fig. 9(a) and (b) is relative to the ULA configurations $\mathbf{z}_1 = [0.50 \ 1.00] \lambda$ and $\mathbf{z}_2 = [1.50 \ 0.75 \ 0] \lambda$, while Fig. 9(c) and (d) are relative to the NULA configurations $\mathbf{z}_3 = [0.35, \ 1.00] \lambda$ and $\mathbf{z}_4 = [0.50 \ 1.50] \lambda$. Recall that the shorter NULA \mathbf{z}_3 was intended to increase the spacing between the blind velocities, while the NULA \mathbf{z}_4 was intended to improve the detection performance against the slow targets. The following observations are in order:

- Focusing on the slowest target, moving at $v_b^{(1)} = 1.5\text{m/s}$, we note that the longest array configurations, namely, the ULA \mathbf{z}_2 and the NULA \mathbf{z}_4 , achieve the best detection performance, as evidenced by the lower nominal P_{fa} value required to detect this target.
- Target 2 is detected with satisfactory performance by most array configurations. Specifically, only the ULA \mathbf{z}_2 does not allow detecting this target, due to the presence of a notch replica in its proximity.
- As for target 3, moving at $v_b^{(3)} = -13\text{m/s}$, the detection performance sensibly depends on the width and positions of the notch replicas. On the one hand, the ULA \mathbf{z}_1 and the NULA \mathbf{z}_4 allow detecting this target with satisfactory performance. Conversely, both the ULA \mathbf{z}_2 and the NULA \mathbf{z}_3 have the first replica of the notch in its proximity. Despite this, the NULA \mathbf{z}_3 still achieves satisfactory detection performance against target 3, thanks to its narrower cancelation notch, which results from its higher global length compared to \mathbf{z}_2 .
- Finally, the target moving at $v_b^{(4)} = 16\text{m/s}$ is detected with satisfactory performance by all the array configurations, since none of the arrays shows any notch in its proximity.

In conclusion, the DVB-T based simulations, obtained by generating the clutter echoes as the signal scattered by a large set of angularly distributed scatterers and using realistic continuous waveforms, confirms the results of the simplified theoretical analysis based on statistical clutter description and ideal waveforms. In particular, it showed that the PC detectors operates effectively against the simulated scenario with both ULA and NULA arrays. Moreover, this analysis confirms that ULA configurations are affected by generally larger cancelation notches and smaller unambiguous velocity sectors. This affects the detection performance on some of the targets of interest. Conversely, the flexibility of the nonuniform spatial sampling provided by NULA configurations allows to achieve overall better performance on the whole velocity sector of interest. Thus, the realistic simulation analysis

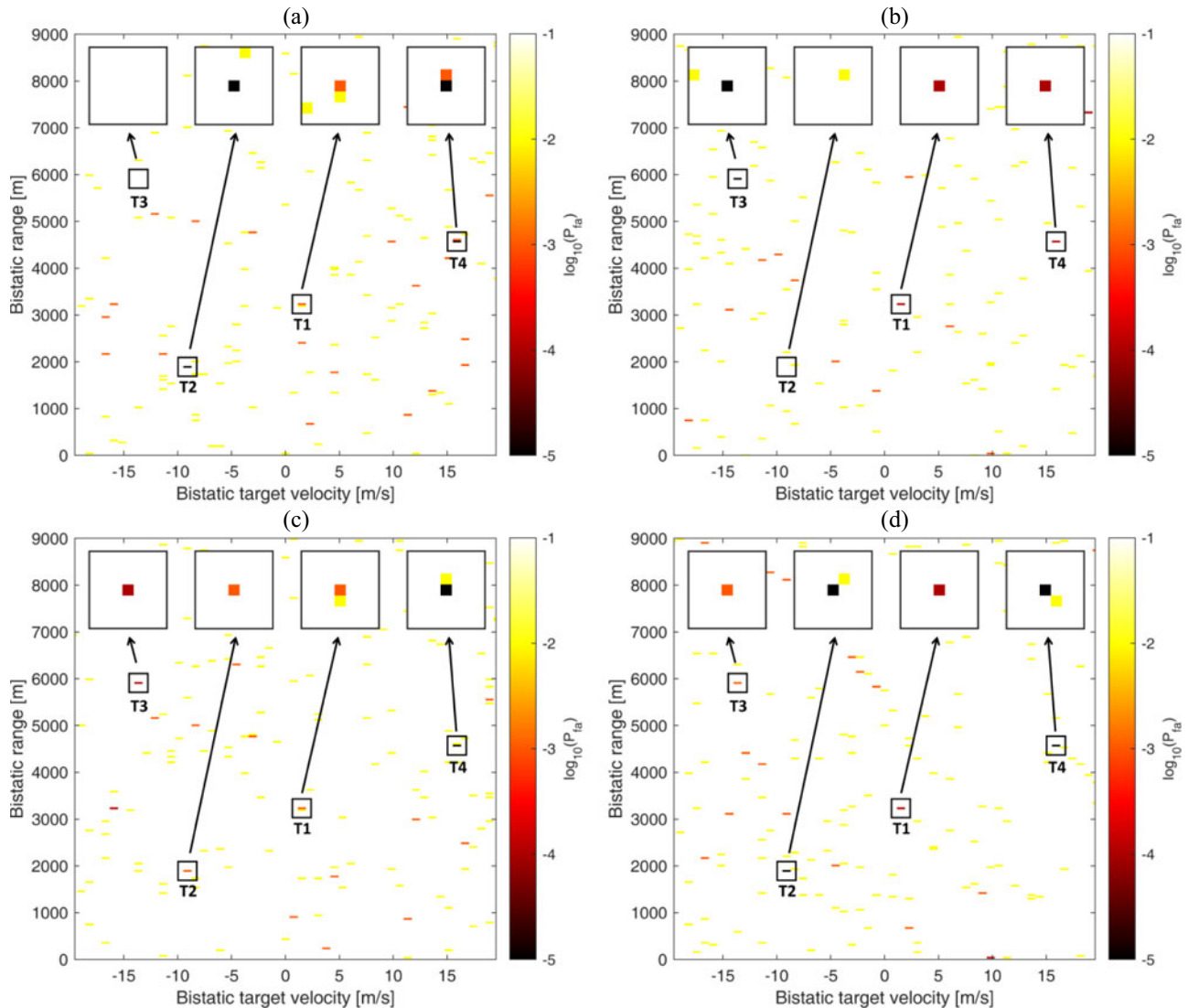


Figure 9. Minimum P_{fa} required to detect each bin using the PC detector: (a) $z_1 = [0.50 \ 1.00] \lambda$; (b) $z_2 = [0.75 \ 1.50] \lambda$; (c) $z_3 = [0.35 \ 1.00] \lambda$; and (d) $z_4 = [0.50 \ 1.50] \lambda$.

confirms the results of “Case study: passive radar system based on DVB-T”.

Conclusions

In this paper, we studied the case of a passive radar system mounted on a moving platform. Specifically, we addressed the problem of clutter suppression, which is a particularly critical task, due to the spread in Doppler of the clutter returns, working on two different but entwined fronts.

On the one hand, based on the signal model derived in “System geometry and signal model”, we proposed three detection schemes, deriving from the generalized LRT: an FC detector, a PC detector, and an APC detector. Each of the detectors has been recognized to consist in a specific combination of the output of N nonadaptive DPCA-like filters. Each of the N DPCA-like filters has a clutter notch with different characteristics, and their combinations allow to have a good response for target moving at the different velocities. They are especially appealing for low-cost, lightweight, and compact systems that can be installed on a moving platform, allowing

to detect moving targets against clutter and noise without requiring the estimation and inversion of the CCM of STAP techniques.

From the system designs perspective, we explored the use of NULA configurations at receive to trade-off the notch width and the spacing between its replicas, without increasing the number of employed sensors. The joint use of nonadaptive processing schemes and NULA configurations allowed to preserve the inherent advantages of passive radars, namely low costs, limited complexity, and ease of deployment.

The comparative performance analysis between ULA and NULA configurations shows that the PC detector, despite its significantly lower computational load, achieves performance very close to the FC detector, requiring intensive computations, when operating together with an ULA. Leveraging the NULA setup to either narrow down the clutter cancellation notch width or increase the spacing between blind velocities causes the PC scheme to operate with limited yet appreciable losses compared to the FC scheme. Hence, the combination of NULA and PC detector, which provides a sensor with the mostly reduced hardware and power absorption requirements adequate for a low-cost, lightweight sensor, must

tolerate some limited detection losses. When this compromise is not acceptable, solutions involving slightly increased hardware or computation can be obtained by either combining an NULA configuration with the FC detector or a ULA configuration with more antenna elements with the PC detector.

Clearly, the target detection performance could be negatively affected by the presence of a model mismatch. However, the results obtained against the simulated scenario of a DVB-T-based passive radar provide encouraging results. As a matter of fact, as detailed in “Case study: passive radar system based on DVB-T”, the clutter signal is simulated as the superposition of the returns from stationary scatterers, and thus it does not rely on the signal model derived in “System geometry and signal model”. Despite this, each of the proposed processing schemes allows to achieve almost perfect clutter suppression.

Future research lines will include the experimental validation of the proposed processing techniques and design strategies in order to investigate their robustness in real-world scenarios. This in turn will require the removal of some of the assumptions made in developing the considered model. Specifically, the perfect DPCA condition, essential for achieving perfect clutter suppression, imposes a severe quantization constraint on the array inter-element distances. As a matter of fact, for a fixed platform velocity and when the batch duration is equal to the OFDM symbol duration, only a handful of NULA configurations allows to guarantee the perfect DPCA condition. Therefore, our future research endeavors will be focused on introducing a flexible batching strategy, independent of the OFDM symbol structure, to decouple the array design from the processing, thus unlocking the full potential of NULA configurations.

Acknowledgements This work was partially supported by the European Union under the Italian National Recovery and Resilience Plan (NRRP) of NextGenerationEU, partnership on “Telecommunications of the Future” (PE00000001 - program “RESTART”), CUP B53C22004050001 - D.D. n.1549 del 11/10/2022.

Competing interests. The authors report no conflict of interest.

List of abbreviations

APC apodized partially coherent
 CCM clutter covariance matrix
 CNR clutter-to-noise power ratio
 CPI coherent processing interval
 CW continuous wave
 DCM disturbance covariance matrix
 DPCA displaced phase center antennas
 DVB-T digital video broadcasting – terrestrial
 FC fully coherent
 ICM internal clutter motion
 NULA nonuniform linear array
 OFDM orthogonal frequency-division multiplexing
 PC partially coherent
 PRF pulse repetition frequency
 Rx receiver
 SCNR signal-to-clutter-and-noise power ratio
 SNR signal-to-noise power ratio
 STAP space-time adaptive processing
 Tx transmitter
 ULA uniform linear array

References

1. **Palmer J, Cristallini D and Kuschel H** (2015) Opportunities and current drivers for passive radar research. In *2015 IEEE Radar Conference*, Johannesburg, South Africa, 145–150.
2. **Ulander LMH, Fröling P, Gustavsson A, Ragnarsson R and Stenström G** (2015) VHF/UHF bistatic and passive SAR ground imaging. In *2015 IEEE Radar Conference (RadarCon)*, Arlington, VA, 0669–0673.
3. **Gromek D, Kulpa K and Samczynski P** (2016) Experimental results of passive SAR imaging using DVB-T illuminators of opportunity. *IEEE Geoscience and Remote Sensing Letters* **13**(8), 1124–1128.
4. **Fang Y, Atkinson G, Sayin A, Chen J, Wang P, Antoniou M and Cherniakov M** (2020) Improved passive SAR imaging with DVB-T transmissions. *IEEE Transactions on Geoscience and Remote Sensing* **58**(7), 5066–5076.
5. **Kulpa K, Malanowski M, Samczynski P and Dawidowicz B** (2011) The concept of airborne passive radar. In *2011 Microwaves, Radar and Remote Sensing Symposium*, Kiev, Ukraine, 267–270.
6. **Brown J, Woodbridge K, Griffiths H, Stove A and Watts S** (2012) Passive bistatic radar experiments from an airborne platform. *IEEE Aerospace and Electronic Systems Magazine* **27**(11), 50–55.
7. **Dawidowicz B, Kulpa K, Malanowski M, Misiurewicz J, Samczynski P and Smolarczyk M** (2012) DPCA detection of moving targets in airborne passive radar. In *IEEE Transactions on Aerospace and Electronic Systems*, 1347–1357, April.
8. **Dawidowicz B, Samczynski P, Malanowski M, Misiurewicz J and Kulpa KS** (2012) Detection of moving targets with multichannel airborne passive radar. *IEEE Aerospace and Electronic Systems Magazine* **27**(11), 42–49.
9. **Wojaczek P, Colone F, Cristallini D and Lombardo P** (2019) Reciprocal filter-based STAP for passive radar on moving platforms. *IEEE Transactions on Aerospace and Electronic Systems* **55**(2), 967–988.
10. **Blasone GP, Colone F, Lombardo P and Cristallini D** (2020) Passive radar DPCA schemes with adaptive channel calibration. *IEEE Transactions on Aerospace and Electronic Systems* **56**(5), 4014–4034.
11. **Quirini A, Blasone GP, Colone F and Lombardo P** (2022) An apodization approach for passive GMTI radar with non-uniform linear arrays. In *2022 19th European Radar Conference (EuRAD)*, Milan, Italy, 109–112.
12. **Quirini A, Blasone GP, Colone F and Lombardo P** (2022) Non-uniform linear arrays for target detection and DoA estimation in passive radar STAP. In *2022 23rd International Radar Symposium (IRS)*, Gdansk, Poland, 224–228.
13. **Quirini A, Blasone GP, Colone F and Lombardo P** (2022) A simple NULA design strategy for target detection and DoA estimation in mobile passive radar. In *International Conference on Radar Systems (RADAR 2022), Hybrid Conference*, Edinburgh, UK.
14. **Griffiths HD and Baker CJ** (2022) *An Introduction to Passive Radar*. Artech House.
15. **Lombardo P and Colone F** (2012) Advanced processing methods for passive bistatic radar systems. In W. L. Melvin and J. A. (eds), *Scheer Principles of Modern Radar: Advanced Radar Techniques*. Rijeka, Croatia: SciTech, 739–821.
16. **Klemm R** (2002) *Principles of Space-Time Adaptive Processing*, 3rd edn. IET.
17. **Brennan LE and Reed IS** (1973) Theory of adaptive radar. *IEEE Transactions on Aerospace and Electronic Systems* **AES-9**, 237–252.
18. **Ward J** (1994) Space-time adaptive processing for airborne radar. Technical Report 1015, Lincoln Laboratory, Massachusetts Institute of Technology, Lexington, MA.
19. **Guerci JR** (2003) Space-time adaptive processing for radar. *Artech House Radar Library*. <https://ieeexplore.ieee.org/document/9106101>
20. **Melvin WL** (2004) A STAP overview. *IEEE Aerospace and Electronic Systems Magazine* **19**(1), 19–35.
21. **Lombardo P** (1998) Data selection strategies for radar space time adaptive processing. In *Proceedings of the 1998 IEEE Radar Conference, RADARCON'98. Challenges in Radar Systems and Solutions (Cat. No. 98CH36197)*, Dallas, TX, USA, 201–206.
22. **Lombardo P, Colone F and Pastina D** (2006) Monitoring and surveillance potentialities obtained by splitting the antenna of the COSMO-SkyMed SAR into multiple sub-apertures. In *IEE Proceedings-Radar, Sonar and Navigation*, vol. 153, 104–116.
23. **Shrader W and Hansen VG** (2008) MTI radar. In M. I. Skolnik (ed), *Radar Handbook*, 3rd edn. McGraw-Hill.

Appendix A

To derive the expressions for the false alarm probability P_{fa} and the detection probability P_d for the PC detector, we proceed as follows. First, we recall that the decision variable is obtained as follows:

$$y_{PC} = \mathbf{y}^H \mathbf{y} = \boldsymbol{\chi}^H \left[\mathbf{I}_N - \frac{1}{N} [1_N 1_N^H] \right] \boldsymbol{\chi} \tag{45}$$

where $\boldsymbol{\chi}$ ($N \times 1$) is the generic Doppler bin of the Fourier-transformed data vector $FFT(\mathbf{x})$, ($NP \times 1$). By definition, we have

$$P_{fa} = \int_T p_{y_{PC}}(y|H_0) dy \tag{46}$$

and

$$P_d = \int_T p_{y_{PC}}(y|H_1) dy. \tag{47}$$

where $p_{y_{PC}}(y|H_i)$ is the probability density function of the random variable y_{PC} under the hypothesis H_i . To derive the probability density function $p_{y_{PC}}(y) = p_{y_{PC}}(y|H_i)$, we resort to the moment-generating function, defined as follows:

$$M_{y_{PC}}(s) = \mathbf{E} \{ e^{sy_{PC}} \} = \int_{-\infty}^{+\infty} e^{sy} p_{y_{PC}}(y) dy \tag{48}$$

To derive the moment-generating function $M_{y_{PC}}(s)$, we define the auxiliary random variable \mathbf{Z} , ($N \times 1$), obtained from $\boldsymbol{\chi}$ by applying the following transformation:

$$\mathbf{Z} = \begin{bmatrix} z_0 \\ \mathbf{Z}_\perp \end{bmatrix} = \mathbf{D}^H \boldsymbol{\chi}. \tag{49}$$

The transformation matrix \mathbf{D} can be any unitary transform (e.g., the DFT matrix) such that

$$\mathbf{D} = [\mathbf{v} \quad \mathbf{V}_{N-1}] \tag{50}$$

where the first column is the unit vector $\mathbf{v} = \frac{1}{\sqrt{N}} \mathbf{1}_N$ and the remaining $N - 1$ columns \mathbf{V}_{N-1} are such that the columns of \mathbf{D} are an orthonormal basis for \mathbb{R}^N . Based on these observations, we have

$$\begin{aligned} \mathbf{Z} &= \begin{bmatrix} z_0 \\ \mathbf{Z}_\perp \end{bmatrix} = \mathbf{D}^H \boldsymbol{\chi} = \begin{bmatrix} \frac{1}{\sqrt{N}} \mathbf{1}_N^H \\ \mathbf{V}_{N-1}^H \end{bmatrix} \boldsymbol{\chi} = \\ &= \begin{bmatrix} \frac{1}{\sqrt{N}} & \frac{1}{\sqrt{N}} \mathbf{1}_{N-1}^H \\ \mathbf{u} & \mathbf{U}_{N-1}^H \end{bmatrix} \boldsymbol{\chi} \end{aligned} \tag{51}$$

This allows us to rewrite the decision variable y_{abs} in terms of \mathbf{Z}_\perp as follows:

$$\begin{aligned} y_{PC} &= \boldsymbol{\chi}^H \left[\mathbf{I}_N - \frac{1}{N} [1_N 1_N^H] \right] \boldsymbol{\chi} = \\ &= \boldsymbol{\chi}^H \begin{bmatrix} 1 - \frac{1}{N} & & -\frac{1}{N} \mathbf{1}_{N-1}^H \\ -\frac{1}{N} \mathbf{1}_{N-1} & \mathbf{I}_{N-1} - \frac{1}{N} \mathbf{1}_{N-1} \mathbf{1}_{N-1}^H & \end{bmatrix} \boldsymbol{\chi} = \\ &= \boldsymbol{\chi}^H \begin{bmatrix} \mathbf{u}^H \\ \mathbf{U}_{N-1}^H \end{bmatrix} \begin{bmatrix} \mathbf{u} & \mathbf{U}_{N-1}^H \end{bmatrix} \boldsymbol{\chi} = \\ &= \boldsymbol{\chi}^H \mathbf{V}_{N-1} \mathbf{V}_{N-1}^H \boldsymbol{\chi} = \mathbf{Z}_\perp^H \mathbf{Z}_\perp \end{aligned} \tag{52}$$

Based on this, we can now derive the moment-generating function as follows:

$$\begin{aligned} M_{y_{PC}}(s) &= \int_{-\infty}^{+\infty} e^{sy} p_{y_{PC}}(y) dy \\ &= \int_{-\infty}^{+\infty} e^{s \mathbf{Z}_\perp^H \mathbf{Z}_\perp} p(\mathbf{Z}_\perp) d\mathbf{Z}_\perp \\ &= \int \frac{1}{\pi^{N-1} |C_{Z_\perp}|} e^{s \mathbf{Z}_\perp^H \mathbf{Z}_\perp} e^{-(\mathbf{Z}_\perp - \bar{\mathbf{Z}}_\perp)^H C_{Z_\perp}^{-1} (\mathbf{Z}_\perp - \bar{\mathbf{Z}}_\perp)} d\mathbf{Z}_\perp \end{aligned} \tag{53}$$

By defining the vector $\mathbf{c} = [C_{Z_\perp}^{-1} - s\mathbf{I}_{N-1}]^{-1} C_{Z_\perp}^{-1} \bar{\mathbf{Z}}_\perp$ of size $(N - 1 \times 1)$, we can rewrite the exponent as follows:

$$\begin{aligned} &s \mathbf{Z}_\perp^H \mathbf{Z}_\perp - (\mathbf{Z}_\perp - \bar{\mathbf{Z}}_\perp)^H C_{Z_\perp}^{-1} (\mathbf{Z}_\perp - \bar{\mathbf{Z}}_\perp) = \\ &= s \mathbf{Z}_\perp^H \mathbf{Z}_\perp - \mathbf{Z}_\perp^H C_{Z_\perp}^{-1} \mathbf{Z}_\perp + \mathbf{Z}_\perp^H C_{Z_\perp}^{-1} \bar{\mathbf{Z}}_\perp + \bar{\mathbf{Z}}_\perp^H C_{Z_\perp}^{-1} \mathbf{Z}_\perp - \bar{\mathbf{Z}}_\perp^H C_{Z_\perp}^{-1} \bar{\mathbf{Z}}_\perp = \\ &= -(\mathbf{Z}_\perp - \mathbf{c})^H [C_{Z_\perp}^{-1} - s\mathbf{I}_{N-1}] (\mathbf{Z}_\perp - \mathbf{c}) - \bar{\mathbf{Z}}_\perp^H C_{Z_\perp}^{-1} \bar{\mathbf{Z}}_\perp + \\ &\quad \mathbf{c}^H [C_{Z_\perp}^{-1} - s\mathbf{I}_{N-1}] \mathbf{c} = \\ &= -(\mathbf{Z}_\perp - \mathbf{c})^H [C_{Z_\perp}^{-1} - s\mathbf{I}_{N-1}] (\mathbf{Z}_\perp - \mathbf{c}) + K(s) \end{aligned} \tag{54}$$

with

$$K(s) = -\bar{\mathbf{Z}}_\perp^H C_{Z_\perp}^{-1} \bar{\mathbf{Z}}_\perp + \mathbf{c}^H [C_{Z_\perp}^{-1} - s\mathbf{I}_{N-1}] \mathbf{c} \tag{55}$$

and recalling that the area of the probability density function

$$\int_{-\infty}^{+\infty} \frac{1}{\pi^{N-1} |C_{Z_\perp}^{-1} - s\mathbf{I}_{N-1}|} e^{-(\mathbf{Z}_\perp - \mathbf{c})^H [C_{Z_\perp}^{-1} - s\mathbf{I}_{N-1}] (\mathbf{Z}_\perp - \mathbf{c})} d\mathbf{Z}_\perp \tag{56}$$

is equal to one, we obtain

$$M_{y_{PC}}(s) = \frac{1}{|\mathbf{I}_{N-1} - sC_{Z_\perp}|} e^{K(s)}. \tag{57}$$

Finally, we need to derive the expression for C_{Z_\perp} . Specifically, we have

$$\begin{aligned} C_{\mathbf{Z}} &= E \{ \mathbf{Z} \mathbf{Z}^H \} \\ &= E \left\{ \begin{bmatrix} |Z_0|^2 & z_0 \mathbf{Z}_\perp^H \\ \mathbf{Z}_\perp z_0^* & \mathbf{Z}_\perp \mathbf{Z}_\perp^H \end{bmatrix} \right\} \\ &= \begin{bmatrix} \frac{1}{\sqrt{N}} \mathbf{1}_N^H \\ \mathbf{V}_{N-1}^H \end{bmatrix} E \{ \boldsymbol{\chi} \boldsymbol{\chi}^H \} \begin{bmatrix} \frac{1}{\sqrt{N}} & \mathbf{1}_N & \mathbf{V}_{N-1} \end{bmatrix} \\ &= \begin{bmatrix} \frac{1}{N} \mathbf{1}_N^H C_x \mathbf{1}_N & \frac{1}{\sqrt{N}} \mathbf{1}_N^H C_x \mathbf{V}_{N-1} \\ \frac{1}{\sqrt{N}} \mathbf{V}_{N-1}^H C_x \mathbf{1}_N & \mathbf{V}_{N-1}^H C_x \mathbf{V}_{N-1} \end{bmatrix}, \end{aligned} \tag{58}$$

so that

$$C_{Z_\perp} = E \{ \mathbf{Z}_\perp \mathbf{Z}_\perp^H \} = \mathbf{V}_{N-1}^H C_x \mathbf{V}_{N-1}. \tag{59}$$

Under the hypotheses H_1-H_3 , we have

$$C_x = \sigma_N^2 (\alpha \mathbf{I}_N + \beta \mathbf{1}_N \mathbf{1}_N^H) \tag{60}$$

so that

$$\begin{aligned} C_{Z_\perp} &= \mathbf{V}_{N-1}^H C_x \mathbf{V}_{N-1} = \\ &= \alpha \mathbf{V}_{N-1}^H \mathbf{V}_{N-1} + \beta \mathbf{V}_{N-1}^H \mathbf{1}_N \mathbf{1}_N^H \mathbf{V}_{N-1} = \\ &= \alpha \mathbf{I}_{N-1}. \end{aligned} \tag{61}$$

Therefore, we can rewrite equation (55) as follows:

$$K(s) = \left(\frac{s}{1 - \alpha s} \right) \bar{\mathbf{Z}}_\perp^H \bar{\mathbf{Z}}_\perp \tag{62}$$

Finally, we can derive P_{fa} and P_d by differentiating the hypotheses H_0 and H_1 .

Under the hypothesis H_0 , we have $\bar{\mathbf{Z}}_\perp = 0$, which yields $K(s) = 0$. Thus, the moment-generating function is given as follows:

$$M_{y_{PC}}(s) = \frac{1}{|\mathbf{I}_{N-1} - sC_{Z_\perp}|} = \left(\frac{1}{1 - \alpha s} \right)^{N-1}, \tag{63}$$

which in turn leads to the following probability density function:

$$p_{y_{PC}}(y|H_0) = \frac{1}{(N-2)! \alpha^N} y_{PC}^{N-1} e^{-\frac{y_{PC}}{\alpha}} \tag{64}$$

Hence, the false alarm probability is obtained as follows:

$$\begin{aligned} P_{fa} &= \int_T p_{y_{PC}}(y|H_0) dy_{PC} = \\ &= \int_T \frac{1}{(N-2)!} \frac{1}{\alpha^N} y_{PC}^{N-1} e^{-\frac{y_{abs}}{\alpha}} dy_{PC} = \\ &= \frac{1}{(N-2)!} \gamma \left(\frac{T}{\alpha}, N-1 \right) \end{aligned} \tag{65}$$

where $\gamma(x, a)$ is the upper incomplete gamma function. Assuming a noise input power of σ_N^2 and setting $\alpha = \frac{N-1}{N}$ to keep the noise output power

unchanged, we finally obtain

$$P_{fa} = \frac{1}{(N-2)!} \gamma \left(\frac{(N-1)T}{N\sigma_N^2}, N-1 \right). \tag{66}$$

The probability of detection P_d can be derived in a similar way. Specifically, under the hypothesis H_0 , we have $\bar{\mathbf{Z}}_{\perp} \neq 0$, which yields $K(s) = \left(\frac{s}{1-\alpha s}\right) \bar{\mathbf{Z}}_{\perp}^H \bar{\mathbf{Z}}_{\perp} = \left(\frac{s}{1-\alpha s}\right) \xi$. Thus, the moment-generating function is now given by

$$M_{y_{PC}}(s) = \frac{1}{(1-\alpha s)^N} e^{\frac{s}{1-\alpha s} \xi}, \tag{67}$$

which in turn leads to the following probability density function:

$$p_{y_{PC}}(y|H_1) = \frac{1}{\alpha} e^{-\frac{r_C + \xi}{\alpha}} \left(\frac{r_C}{\xi}\right)^{\frac{N-1}{2}} I_{N-1} \left(2\sqrt{\xi \frac{r_C}{\alpha^2}} \right) \tag{68}$$

Hence, the probability of detection is obtained as follows:

$$P_d = \int_T^{\infty} p_{y_{PC}}(y|H_1) dy_{abs} = \int_T^{\infty} \frac{1}{\alpha} e^{-\frac{y_{PC} + \xi}{\alpha}} \left(\frac{y_{PC}}{\xi}\right)^{\frac{N-1}{2}} I_{N-1} \left(2\sqrt{\xi \frac{y_{PC}}{\alpha^2}} \right) dy_{abs} \tag{69}$$

By recognizing the Marcum-Q function of order $N-1$, equation (69) can be rewritten as follows:

$$P_d = Q \left(\sqrt{\frac{(N-1)2\xi}{N\sigma_N^2}}, \sqrt{\frac{(N-1)2T^2}{N\sigma_N^2}}, N-1 \right) \tag{70}$$

Appendix B

To derive the approximate expressions for the false alarm probability P_{fa} and the detection probability P_d for the APC detector, we proceed as follows.

First, we recall that the decision variable is obtained as follows:

$$y_{APC} = \max(\mathbf{y}^* \odot \mathbf{y}) \tag{71}$$

Note that the vector \mathbf{X} collects N independent complex normal random variables. By recalling the definition of \mathbf{y}

$$\mathbf{y} = \frac{1}{\sigma_n^2} \mathbf{\Pi}_N \mathbf{X}, \tag{72}$$

we note that the vector \mathbf{y} collects N complex normal random variables as well. However, the matrix $\mathbf{\Pi}_N = \mathbf{I}_N - \frac{1}{N} [\mathbf{1}_N \mathbf{1}_N^H]$ is such that the N random variables in \mathbf{y} are no longer independent. Specifically, the last element of \mathbf{y} can be written as a linear combination of the previous $N-1$ elements:

$$y[N-1] = - \sum_{n=0}^{N-2} y[n]. \tag{73}$$

We denote the real and imaginary components of \mathbf{y} as $Y^R[n] \sim \mathcal{N}(\mu_n^R, \sigma_N^2/2)$ and $Y^I[n] \sim \mathcal{N}(\mu_n^I, \sigma_N^2/2)$.

Note that the detector in equation (71) evaluates the maximum of the absolute squared values of each component of \mathbf{y} . Therefore, it is convenient to define the random variables $Y_n = Y^R[n]^2 + Y^I[n]^2$ and $Z = \max_n(Y_n)$.

Under the hypothesis H_0 , we have $\mu_n^R = \mu_n^I = 0, \forall n = 0 \dots N-1$. Therefore, the random variable Y_n is exponentially distributed, namely $Y_n \sim \text{expnd}(1/\sigma_N^2)$, and its cumulative distribution function $F_{Y_n}(y)$ is given as follows:

$$F_{Y_n}(y) = \text{Prob}\{Y_n \leq y\} = (1 - e^{-y/\sigma_N^2}). \tag{74}$$

Furthermore, for the cumulative distribution function $F_Z(z)$ of Z , we have

$$\begin{aligned} F_Z(z) &= \text{Prob}\{Z \leq z\} = \\ &= \text{Prob}\left\{\max_n Y_n \leq z\right\} = \\ &= \text{Prob}\{Y_0 \leq z, Y_1 \leq z, \dots, Y_{N-1} \leq z\} \end{aligned} \tag{75}$$

A lower bound for $F_Z(z)$ can thus be obtained as follows:

$$F_Z(z) \geq \prod_{n=0}^{N-1} \text{Prob}\{Y_n \leq z\} = \left(1 - e^{-\frac{z}{\sigma_N^2}}\right)^N, \tag{76}$$

since the probability of N joint events is always greater than or equal to the product of the probabilities of the individual events (with the equality holding when the N events are independent). Finally, the false alarm probability can be derived as follows:

$$P_{fa} = \int_T^{+\infty} p_Z(z) dz = 1 - \int_{-\infty}^T p_Z(z) dz = 1 - F_Z(T) \tag{77}$$

which leads to the following upper bound:

$$P_{fa} \lesssim 1 - (1 - e^{-T/\sigma_N^2})^N \tag{78}$$

From the performance analysis carried out in the previous sections, we note that this upper bound is indeed a good approximation for the actual P_{fa} .

Under the hypothesis H_1 , we can proceed in a similar way to derive the P_d . In general, we have $\mu_n^R \neq \mu_n^I \neq 0$, so that the variable $\frac{2Y_n}{\sigma_N^2}$ is now a non-central chi-square, namely $\frac{2Y_n}{\sigma_N^2} \sim \chi_2^2 \left(\frac{\mu_n^R + \mu_n^I}{\sigma_N^2/2}\right)$. Therefore, the cumulative distribution function $F_{\frac{2Y_n}{\sigma_N^2}}\left(\frac{2y}{\sigma_N^2}\right)$ is given as follows:

$$F_{\frac{2Y_n}{\sigma_N^2}}\left(\frac{2y}{\sigma_N^2}\right) = 1 - Q_1 \left(\sqrt{\frac{\mu_n^R + \mu_n^I}{\sigma_N^2/2}}, \sqrt{\frac{2y}{\sigma_N^2}} \right). \tag{79}$$

Hence, for the variable $Z = \max_n(Y_n)$ denoting the maximum of the N variables $\frac{2Y_n}{\sigma_N^2}$, we have

$$\begin{aligned} F_Z(z) &= \text{Prob}\{Z \leq z\} = \\ &= \text{Prob}\left\{\max_n \frac{2Y_n}{\sigma_N^2} \leq z\right\} = \\ &= \text{Prob}\left\{\frac{2Y_0}{\sigma_N^2} \leq z, \frac{2Y_1}{\sigma_N^2} \leq z, \dots, \frac{2Y_{N-1}}{\sigma_N^2} \leq z\right\} \end{aligned} \tag{80}$$

As before, a lower bound for latter expression is obtained by assuming the independence of the N random variables Y_k :

$$\begin{aligned} F_Z(z) &> \prod_{n=0}^{N-1} \text{Prob}\left\{\frac{2Y_n}{\sigma_N^2} \leq z\right\} = \\ &= \prod_{n=0}^{N-1} \left(1 - Q_1 \left(\sqrt{\frac{2(\mu_n^R + \mu_n^I)}{\sigma_N^2}}, \sqrt{\frac{2z}{\sigma_N^2}} \right)\right) \end{aligned} \tag{81}$$

Finally, the probability of detection can be derived as follows:

$$P_d = \int_T^{+\infty} p_Z(z) dz = 1 - \int_{-\infty}^T p_Z(z) dz = 1 - F_Z(T) \tag{82}$$

which leads to

$$P_d < 1 - \prod_{n=0}^{N-1} \left(1 - Q \left(\sqrt{\frac{2(\mu_n^R + \mu_n^I)}{\sigma_N^2}}, \sqrt{\frac{2T}{\sigma_N^2}} \right)\right) \tag{83}$$

In this case, the derived expression is not a good approximation for the actual P_d , but it represents a useful upper bound for the performance under the hypothesis H_1 .



Andrea Quirini received the B.Sc. and M.Sc. degrees (*cum laude*) in telecommunications engineering from the Sapienza University of Rome, Rome, Italy, in July 2018 and October 2020, respectively. He also received a double degree in electrical and computer engineering from the Georgia Institute of Technology, Atlanta, Georgia, in May 2020. He is currently working toward the Ph.D. degree in radar and remote sensing within the

Department of Information Engineering, Electronics and Telecommunications, Sapienza University of Rome. His main research interests include OFDM radar, clutter suppression in multichannel passive radar on moving platforms, and nonuniform linear array signal processing. He has been a recipient of the second prize in the Young Scientist Award of the 2022 23rd International Radar Symposium (October 2022, Gdansk).



Giovanni Paolo Blasone received the B.Sc. degree (*cum laude*) in electronic engineering and the M.Sc. degree (*cum laude*) in telecommunications engineering from the Sapienza University of Rome, Rome, Italy, in 2012 and 2016, respectively. He also received his Ph.D. degree in radar and remote sensing from the Department of Information Engineering, Electronics and Telecommunications, Sapienza University of

Rome in 2021. His main research interests include adaptive signal processing for multichannel radar systems and passive radar GMTI. He has been involved in research projects funded by the Italian Space Agency, the Italian Ministry of Research, and the radar industry. He was a finalist in the Student Paper Competition of the 2020 IEEE International Radar Conference (Washington, DC, USA) and in the 3MT contest of the 2020 IEEE Radar Conference (Florence, Italy).



Fabiola Colone received the degree in Telecommunications Engineering and the Ph.D. degree in Remote Sensing from Sapienza University of Rome, Italy, in 2002 and 2006, respectively. She joined the DIET Department of Sapienza University of Rome as a Research Associate in January 2006. From December 2006 to June 2007, she was a Visiting Scientist at the Electronic and Electrical Engineering Department

of the University College London, London, UK. She is currently a Full Professor at the Faculty of Information Engineering, Informatics, and Statistics of Sapienza University of Rome, where she holds the role of Chair of the degree programs in Communications Engineering. The majority of Dr Colone's research activity is devoted to radar systems and signal processing. She has been involved, with scientific responsibility roles, in research projects funded by the European Commission, the European Defence Agency, the Italian Space Agency, the Italian Ministry of Research, and many radar/ICT companies.

Her research has been reported in over 180 publications in international technical journals, book chapters, and conference proceedings. Dr Colone is co-editor of the book "Radar Countermeasures for Unmanned Aerial Vehicles," IET Publisher. She has been a co-recipient of the 2018 Premium Award for Best Paper in IET Radar, Sonar & Navigation. Since 2017 she has been a member of the Board of Governors of the IEEE Aerospace and Electronic System Society (AESS), where she has served as Vice President for Member Services and Editor in Chief for the IEEE AESS QEB Newsletters. She is an IEEE Senior Member from 2017 and a member of the IEEE AESS Radar System Panel from 2019. Dr Colone is the Associate Editor in Chief for the IEEE Transactions on Radar Systems. She was Associate Editor for the IEEE Transactions on Signal Processing from 2017 to 2020 and is a member of the Editorial Board of the International Journal of Electronics and Communications (Elsevier). She was Technical Co-Chair of the IEEE 2021 Radar Conference (Atlanta, USA) and of the European Radar Conference EuRAD 2022 (Milan, Italy), and she served in the organizing committee and the technical program committee of many international conferences.



Pierfrancesco Lombardo received the degree in electronic engineering and the Ph.D. degree in remote sensing from the University of Rome "La Sapienza," Rome, Italy, in 1991 and 1995, respectively. After serving at the Official Test Centre of the Italian Air Force in 1992, he was an Associate with Birmingham University (UK) and at Defense Research Agency in Malvern, in 1994. In 1995, he was a Research Associate at

Syracuse University (NY, USA). In 1996, he joined the University of Rome "La Sapienza," where he is presently a Full Professor. He is involved in, and coordinates, research projects funded by European and National Research Agencies and national industries. He leads the "Radar, Remote Sensing and Navigation" group, University of Rome "La Sapienza." He chairs the Cosmo-SkyMed consulting group for the Italian Space Agency. His main research interests include radar adaptive signal processing, radar clutter modeling, radar coherent detection, passive radar and multistatic radar, SAR processing, and radio-localization systems. His research has been reported in over 280 publications in international technical journals and conferences and in five book chapters. Dr Lombardo is a co-recipient of the Barry Carlton award (best paper) of IEEE Transactions on Aerospace and Electronic Systems (AES) in 2001 and of the best paper award for IEEE Transactions on Geoscience and Remote Sensing in 2003. He served in the technical committee of many international conferences on radar systems and signal processing. He was Technical Committee Chairman of the IEEE/ISPRS Workshop on Remote Sensing and Data Fusion over Urban Areas URBAN²2001, Rome, URBAN²2003, Berlin, and URBAN²2005, Tempe (US). He was also Technical Chairman of the IEEE Radar Conference 2008. He has been the Associate Editor for Radar Systems for the IEEE Transactions on AES since June 2001 and Technical Editor for Radar Systems since January 2016. He is a member of the IEEE AES Radar System Panel and the Editorial Board of IET Proceedings on Radar Sonar and Navigation.